

Relaxation dynamics of two interacting electrical double-layers in a 1D Coulomb system

Lucas Varela^{1,2,*}, Sergio Andraus³, Emmanuel Trizac² and Gabriel Téllez¹

¹ Departamento de Física, Universidad de los Andes, Bogotá, Colombia

² Université Paris-Saclay, CNRS, LPTMS, 91405, Orsay, France

³ Graduate School of Physics, The University of Tokyo, Tokyo 113-0033, Japan

E-mail: l.varela10@uniandes.edu.co

Received 17 May 2021, revised 25 June 2021

Accepted for publication 7 July 2021

Published 26 July 2021



CrossMark

Abstract

We consider an out-of-equilibrium one-dimensional model for two electrical double-layers. With a combination of exact calculations and Brownian dynamics simulations, we compute the relaxation time (τ) for an electroneutral salt-free suspension, made up of two fixed colloids, with N neutralizing mobile counterions. For N odd, the two double-layers never decouple, irrespective of their separation L ; this is the regime of like-charge attraction, where τ exhibits a diffusive scaling in L^2 for large L . On the other hand, for even N , L no longer is the relevant length scale for setting the relaxation time; this role is played by the Bjerrum length. This leads to distinctly different dynamics: for N even, thermal effects are detrimental to relaxation, increasing τ , while they accelerate relaxation for N odd. Finally, we also show that the mean-field theory is recovered for large N and moreover, that it remains an operational treatment down to relatively small values of N ($N > 3$).

Keywords: electrical double layer, stochastic dynamics, Coulomb potential

(Some figures may appear in colour only in the online journal)

1. Introduction

The contact between a charged surface or colloid particle with an ionic solution is known to create an electrical double-layer: a diffuse counterion cloud around the charged interface which extends a distance typically in the colloidal range, from molecular dimensions to the micrometer scale [1, 2]. The study of electric double-layers is an active research topic due to their importance to understand phenomena such as like-charge attraction [3, 4], ion transport in biological membranes [5] or nanofluidics [6–8]. Furthermore, they play a significant role in the design and development of bio-chemical sensors [9], super capacitors [10–13], electric-double-layer-gated transistors [14], water treatment [15], etc.

Electrical double-layers have been studied extensively [1, 16–18]. They were first introduced in 1897 by Helmholtz while investigating electrodes in electrolytes subject to an external potential [19]. In this model, the counterions form a single layer close to the electrode. Then, Gouy [20] and Chapman [21] introduced the concept of a diffuse layer, where the counterion typical position results from the competition between entropic and electrostatic effects. This model was further improved by Stern [22], by assuming that the electrolyte system is made up of two parts: first comes a layer that is strongly bound to the electrode surface (practically immobile) and then follows the diffuse part, where counterions are loosely bound. The study of electrical double-layers displays numerous approaches that quickly increase in difficulty as the model restrictions are relaxed and ingredients are added. The Gouy–Chapman model resorts to a mean-field treatment that assumes weak electrostatic interactions and con-

* Author to whom any correspondence should be addressed.

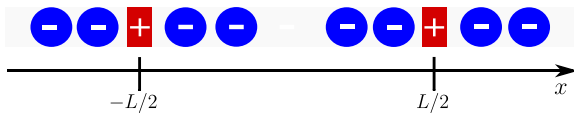


Figure 1. Sketch of an electroneutral system consisting of two interacting electric double-layers, each made of a colloid (rectangle) and 4 counterions (circles). The distance between colloids is L . The interaction between particles is mediated by the 1D Coulomb potential, linear in separation. The dynamics of the counterions is considered and the colloids are treated as static since their time scale is assumed to be much larger than that of the counterions. All particles are point-like and they can ‘cross over’ each other.

siders the ionic fluid as a continuum, discarding discreteness effects. The latter shortcoming can be partly addressed including ionic size effects within a mean-field framework [23–27] (see [28] for a criticism on these approaches, and [29] for a review on mean-field electric double-layers). Using mean-field models is convenient since they may yield analytic expressions. Interestingly, while mean-field techniques fail when the electrostatic coupling increases [30–35], strongly-coupled systems lend themselves to analytical progress [36, 37]. The remaining intermediate regime between weak and strong coupling is mostly accessible through numerics. So far, equilibrium properties mostly have been studied, and results are scarce for time dependent phenomena. The physics of out-of-equilibrium electrical double-layers is primarily described via mean-field and numerical approaches [1, 38–46], with few beyond mean-field contributions [45, 47, 48].

Herein are reported exact and numerical results, within all coupling regimes, for the relaxation time toward equilibrium of two interacting double-layers in one dimension, at a distance L . Such systems have been studied at equilibrium [49–52]. We consider the dynamics of an electroneutral system made of two symmetrically-placed, permeable like-charged colloids and N counterions as shown in figure 1. Due to their larger mass, the colloids are assumed to exhibit a very large time scale for displacement compared to the counterions, hence we consider them to be fixed, and address the dynamics of the diffuse layer. The single counterion case ($N = 1$) allows an analytical solution for the particle density and relaxation time. This subsumes the essential features of the dynamics for any odd number of counterions. Indeed, the parity of N plays an important role, for both static and dynamics properties: if N is even, the large L regime features decoupled neutral entities, with $N/2$ counterions neutralizing each colloid. This is no longer possible for N odd, for which there is always a misfit counterion [51, 53], that plays an important role in what follows. The misfit effect is accurately described by the mean passage of a free diffusing particle in a reduced length approximately given by the colloid separation minus the space taken by the double-layers between the colloids. For even N , the two double-layers form and completely neutralize each colloid. The decoupling between the two moieties, made possible for even N , explains why the relaxation process becomes L independent for large L , in contrast with the odd case.

It is worth pointing out that one-dimensional approaches may be insightful for more realistic systems. As an

illustration, we mention the question of the origin of cement cohesion. In brief, cement, a key binding agent in concrete, is made of layers of calcium-silicate-hydrates (C–H–S) that trap between them a solution made of water and ions [54–56]. While the physical chemistry of cement is complex [54, 55], a simple model for this system is provided by two symmetric uniformly charged plates with counterions between them, where these charges interact pairwise via the 3D Coulomb potential, $1/r$. The fact that counterions are multivalent, and the plates highly charged, brings the cement system in the strong-coupling regime. This triggers like-charge attraction, that is at the origin of cement cohesion. In the strong-coupling regime, when the distance between plates is small enough, all counterions are approximately in the same plane parallel to the plates, so that the dominant force acting on them stems from the plates’ potential. For like-charged plates, this force vanishes, which leads to a uniform density profile, from which the pressure can be readily computed. In this limit, the $N = 1$ ion problem in one dimension exhibits the same equation of state as its three dimensional counterpart [33, 36, 53, 57, 58]. We will begin our discussion with the out of equilibrium analysis for the single counterion case.

The paper is structured as follows. The time evolution of the probability density for one counterion ($N = 1$) is computed analytically in section 2, parameterized by the colloid distance L . The density displays an exponential decay toward equilibrium, which naturally introduces a relaxation time. Then, a scheme is introduced to determine this quantity, from a simulation based on the corresponding Langevin dynamics. The results are in good agreement with exact values. In section 3, the numerical study of the relaxation time is generalized for the many-counterion case, $N > 1$. The role of the parity of N and the symmetry of the initial condition (IC) is discussed, with the former leading to two different behaviors for the relaxation time. In section 4, we study the analytic mean-field treatment of a system at zero colloid separation. We find that this solution serves as a good approximation for the discrete charge system, for a large number of counterions as expected, but more surprisingly already for N as small as 3. Treating the counterions as discrete charges results in exponential relaxation dynamics. This is in contrast to mean-field theory, that features a slower, algebraic decay [1]. We explain below how the two regimes are matched, and show explicitly how mean-field’s accuracy improves, upon increasing the number of counter-ions N . Finally, we investigate numerically in section 5 the first passage time of the middle/misfit counterion between the two double-layers when N is odd, to rationalize the behavior of the relaxation time. We conclude in section 6.

2. One counterion ($N = 1$)

In this section, we consider an electroneutral system made of a single counter-ion ($N = 1$), of charge e and two colloids, each with charge $-e/2$. The colloids have fixed positions: $-L/2$ and $L/2$. These charges interact via the 1D Coulomb potential energy, which for two charges q_1 and q_2 at x_1 and x_2 is

given by

$$V_{\text{ID}}(x_1, x_2) = -\frac{q_1 q_2}{\epsilon} |x_1 - x_2|, \quad (1)$$

where ϵ is the dielectric constant of the medium. This potential leads to a force that does not depend on the inter-charge distance, unlike the two- or three-dimensional result. This can be understood with a three dimensional detour, working out the potential between two infinite uniformly charged plates: each of the plates creates a uniform electric field, and hence a locally linear potential. As a result, the inter-plate potential is exactly of the 1D form [59] of equation (1).

The counterion's position x is ruled by the following overdamped Langevin equation:

$$m\gamma \frac{dx}{dt} = -\frac{d\Phi(x)}{dx} + \sqrt{m\gamma k_B T_{\text{bath}} \xi(t)}, \quad (2)$$

where γ is the damping coefficient, T_{bath} the temperature, m the counterion mass, and $\Phi(x) = V_{\text{ID}}(x, L/2) + V_{\text{ID}}(x, -L/2)$ is the electrostatic potential energy due to the colloids. The stochastic Langevin force $\xi(t)$ is a Gaussian white noise characterized by zero mean $\langle \xi(t) \rangle = 0$, and delta time correlation $\langle \xi(t_1) \xi(t_2) \rangle = 2\delta(t_1 - t_2)$.

There is an important length scale related to the electrostatic interaction, namely the Bjerrum length, which in this one-dimensional context is defined as $l_B = k_B T_{\text{bath}} \epsilon / e^2$. When two e -charges are pushed closer to one another, an energy budget of $k_B T_{\text{bath}}$ corresponds to a relative displacement over a distance l_B . Note that l_B is exactly the inverse of its three dimensional counterpart: this stems from the fact that the 1D Coulomb potential is linear in distance between charges, while it goes like the inverse distance in 3D. Associated to the diffusive dynamics we consider here, we can define a characteristic time scale $\tau_B = l_B^2 / D$ where $D = k_B T_{\text{bath}} / (\gamma m)$ is the diffusion coefficient. In the following, it will prove useful to work with the rescaled units: $\tilde{x} = x / l_B$, $\tilde{t} = t / \tau_B$ and $\tilde{\Phi} = \Phi / (k_B T_{\text{bath}})$; the length and time scales are such that the diffusion coefficient is set to unity in the dimensionless units.

Since the dynamics are given by a Markov process, the time evolution for the probability density function starting at any given time t_0 can be determined with the transition probability $p(x, t | x_0, t_0)$, where $p(x, t_0 | x_0, t_0) = \delta(x - x_0)$, without knowledge of the preceding time evolution. In the following we will set $t_0 = 0$ and avoid writing it explicitly, $p(x, t | x_0) \equiv p(x, t | x_0, 0)$. Equation (2) has an associated Fokker–Planck equation that governs the transition probability p (also known as the propagator, which is nothing but the density of ions):

$$\frac{\partial p(\tilde{x}, \tilde{t})}{\partial \tilde{t}} = \frac{\partial}{\partial \tilde{x}} \left(p(\tilde{x}, \tilde{t}) \frac{\partial \tilde{\Phi}(\tilde{x}, \tilde{L})}{\partial \tilde{x}} \right) + \frac{\partial^2 p(\tilde{x}, \tilde{t})}{\partial \tilde{x}^2}, \quad (3)$$

where the rescaled 1D Coulomb potential $\tilde{\Phi}$ is given by

$$\tilde{\Phi}(\tilde{x}, \tilde{L}) = \begin{cases} \tilde{L}/2 & \text{if } |\tilde{x}| < \tilde{L}/2 \\ |\tilde{x}| & \text{if } |\tilde{x}| > \tilde{L}/2 \end{cases}. \quad (4)$$

Note that when $\tilde{L} = 0$, equation (3) is formally the same Fokker–Planck equation that describes a Brownian motion

with dry friction [60, 61]. We review in appendix A the corresponding solution, which will be relevant in the following sections as a limiting case.

Equation (3) is a forward Fokker–Planck equation that features a piece-wise constant force. It is equipped with boundary condition $p(\tilde{x} \rightarrow \pm\infty, \tilde{t} | \tilde{x}_0) = 0$. It can therefore be solved analytically using an eigenvalue expansion [62]:

$$p(\tilde{x}, \tilde{t} | \tilde{x}_0) = p_\infty(\tilde{x}) + \sum_{\alpha=0,e} \sum_k \frac{u_k^\alpha(\tilde{x}) \nu_k^\alpha(\tilde{x}_0)}{Z_k^\alpha} e^{-\lambda_k^\alpha \tilde{t}} + \sum_{\alpha=0,e} \int_{\frac{1}{4}}^{\infty} d\lambda \frac{u^\alpha(\tilde{x}, \lambda) \nu^\alpha(\tilde{x}_0, \lambda)}{Z^\alpha(\lambda)} e^{-\lambda \tilde{t}}, \quad (5)$$

where u_k^α and u^α are the eigenfunctions of the Fokker–Planck operator (rhs of equation (3)), ν_k^α and ν^α are their adjoint eigenfunctions, and Z_k^α and Z^α the normalization constants. The equilibrium distribution p_∞ is given by:

$$p_\infty(\tilde{x}) = \frac{e^{-\tilde{\Phi}(\tilde{x})}}{Z_\infty} = \frac{e^{-\tilde{\Phi}(\tilde{x}) + \tilde{L}/2}}{\tilde{L} + 2}. \quad (6)$$

The superscript α in equation (5) indicates the parity of the eigenfunctions, which will be discussed in upcoming sections. The explicit expression of the functions and their derivation can be found in appendix B. Note that equation (5) features two different types of terms, corresponding either to discrete eigenvalues (with subscript λ_k) or to a continuous spectrum (the integral terms, involving functions of λ). This aspect will play a key role in the subsequent treatment.

2.1. Analytic dynamics

We investigate here the dynamics of the counterion density $p(\tilde{x}, \tilde{t})$, given that it starts with initial position \tilde{x}_0 . There are two different possibilities for this IC: in the interstitial region between the colloids ($|\tilde{x}_0| \leq \tilde{L}/2$) or outside ($|\tilde{x}_0| > \tilde{L}/2$).

Let us start with the counterion in the space between the two colloids. The initial dynamics is that of a particle in free diffusion, lasting approximately until spread of the density (increasing in $\sqrt{2\tilde{t}}$) reaches the nearest colloid. This behavior can be seen directly in figure 2 where we observe that the density remains left–right symmetric with respect to the counterion's initial position and it starts to become skewed once the nearest colloid is ‘hit’ (located at $\tilde{x} = 5$). This is corroborated in figure 3, which features the dynamics of the average position $\langle x \rangle$ (inset) and the position's variance σ_x^2 : the former is constant, and the latter increases linearly with time until the density ‘hits’ the colloid.

On the other hand, when the counterion starts outside the interstitial region ($|\tilde{x}_0| > \tilde{L}/2$) it initially experiences a constant drift toward the colloids. This causes the particle to move toward the colloids, with a mean position that travels at constant speed. This is seen in the inset of figure 3, where for small times the mean position is a linear function of time when $\tilde{x}_0 > \tilde{L}$. Besides, there is a constant diffusion which is manifested in a linear growth of the position variance ($\sigma_x^2 \sim 2\tilde{t}$, see figure 3). The time during which the drift diffusion occurs lasts approximately until the mean position of the counterion

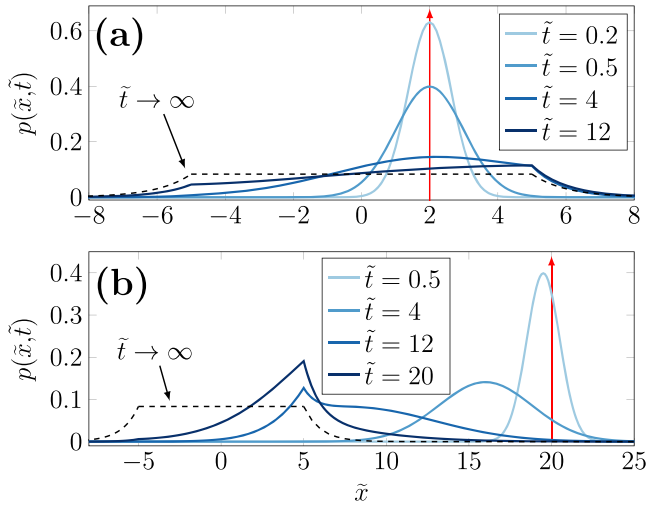


Figure 2. Time evolution of the density $p(\tilde{x}, \tilde{t})$ for a single counterion ($N = 1$), with colloid separation $\tilde{L} = 10$ and localized initial distribution centered at \tilde{x}_0 (red arrows): (a) $\tilde{x}_0 = 2$, and (b) $\tilde{x}_0 = 20$. The equilibrium state ($\tilde{t} \rightarrow \infty$) is given by the dashed lines. In panel (b), the cusp formed at $\tilde{x} = 5$ for $\tilde{t} = 20$ is understood in terms of the wedge potential: to the right of the colloid there is a constant force causing a greater probability flow than from the left side where the counterion undergoes free diffusion.

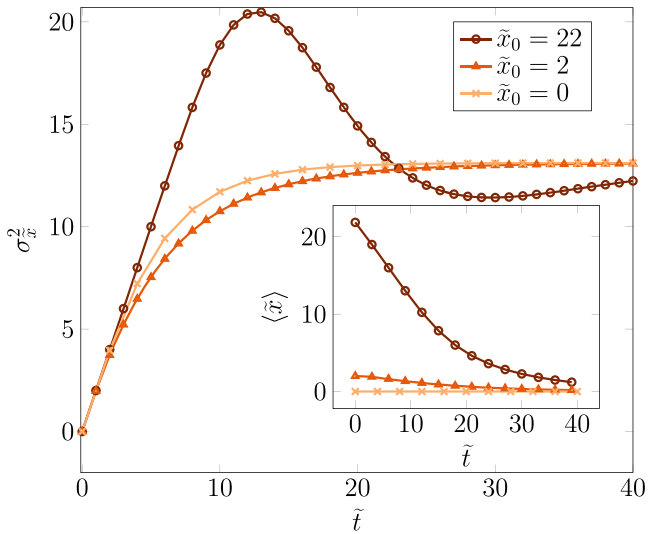


Figure 3. Position variance $\sigma_x^2(\tilde{t})$ of a single counterion $N = 1$ with a localized IC $\tilde{x}_0 = 0, 2, 22$ and colloid separation $\tilde{L} = 10$. Note that for short times $\sigma_x^2(\tilde{t})$ is linear in time $\sigma_x^2(\tilde{t}) \approx 2\tilde{t}$. For $\tilde{x}_0 = 22$ the variance is not monotonous, which happens because the initial position is large enough to allow the regime of linear expansion to overshoot the equilibrium variance. The inset is for the corresponding average position $\langle \tilde{x} \rangle$ for each IC. For large times the average position decays exponentially toward 0, except for the case $\tilde{x}_0 = 0$ where it identically vanishes.

and its nearest colloid are one standard deviation apart. Upon reaching the central region, it has to ultimately accommodate to the asymptotic steady state given by equation (6); hence the non-monotonic behavior of the position variance in figure 3.

We now turn to the asymptotic equilibrium distribution; there is a closed form for the counterion position's average

and variance:

$$\lim_{\tilde{t} \rightarrow \infty} \langle \tilde{x}(\tilde{t}) \rangle = 0, \quad (7)$$

$$\lim_{\tilde{t} \rightarrow \infty} \sigma_x^2(\tilde{t}) = \frac{\tilde{L}^2}{12} + \frac{\tilde{L}}{3} + \frac{4}{3} + \frac{4}{3(\tilde{L} + 2)}. \quad (8)$$

Averages are taken here with respect to the equilibrium distribution p_∞ (equation (6)). Note that for large \tilde{L} , the dominant term is $\tilde{L}^2/12$ which recovers the result of a Brownian particle inside a 1D box of length \tilde{L} .

2.2. Eigenvalues and relaxation time

Equation (5) shows that there is an exponential relaxation toward the equilibrium distribution p_∞ . Therefore, the relaxation time $\tilde{\tau}$ can be defined as the inverse of the decay rate associated to the dominant term in equation (5) for large times. To determine this rate, it is necessary to know the eigenvalue structure of the Fokker–Planck equation (equation (3)) and more precisely the spectral gap (first non-vanishing eigenvalue), which is the inverse of $\tilde{\tau}$. In this section, we explore the \tilde{L} -dependence of the spectrum and consequently of $\tilde{\tau}$.

The spectrum is made of two parts, one discrete and one continuous, which stem from enforcing vanishing boundary conditions at infinity to the eigenfunctions of the Fokker–Planck operator (more details are presented in appendix B). Since the Fokker–Planck equation is formally equivalent to a Schrödinger equation [62], we can also understand the spectrum in terms of quantum mechanics: the discrete and continuous parts correspond to the bounded and unbounded equilibrium states of a single nonrelativistic particle in one dimension, subject to a square well-like potential [63]. The discrete set of eigenvalues $\{\lambda_k\}_k \in [0, 1/4)$ is \tilde{L} -dependent, while the continuous spectrum is the interval $[1/4, \infty)$. The discrete eigenvalues are obtained from solving the following equations subject to the restriction $0 \leq \lambda_k < 1/4$:

$$(1 - \sqrt{1 - 4\lambda_k^o}) \tan(\tilde{L}\sqrt{\lambda_k^o}/2) = 2\sqrt{\lambda_k^o}, \quad (9)$$

$$(\sqrt{1 - 4\lambda_k^e} - 1) \cot(\tilde{L}\sqrt{\lambda_k^e}/2) = 2\sqrt{\lambda_k^e}, \quad (10)$$

where equations (9) and (10) are for odd and even eigenfunctions respectively. Note that the discrete set is non-empty because $\lambda_0 = 0$ is always a solution to equation (10). From equations (9) and (10), it follows that the number of odd (N_{λ^o}) and even (N_{λ^e}) discrete eigenvalues for a given length are:

$$N_{\lambda^o} = \left\lfloor \frac{\tilde{L} - \pi}{4\pi} \right\rfloor + 1, \quad (11)$$

$$N_{\lambda^e} = \left\lfloor \frac{\tilde{L} + \pi}{4\pi} \right\rfloor + 1. \quad (12)$$

From N_{λ^o} and N_{λ^e} we see that discrete eigenvalues emerge as \tilde{L} increases: odd and even eigenvalues appear in an alternating sequence as a function of \tilde{L} with period 2π , such that the second eigenvalue λ_2 is odd and present for $\tilde{L} > 3\pi$, and so on,

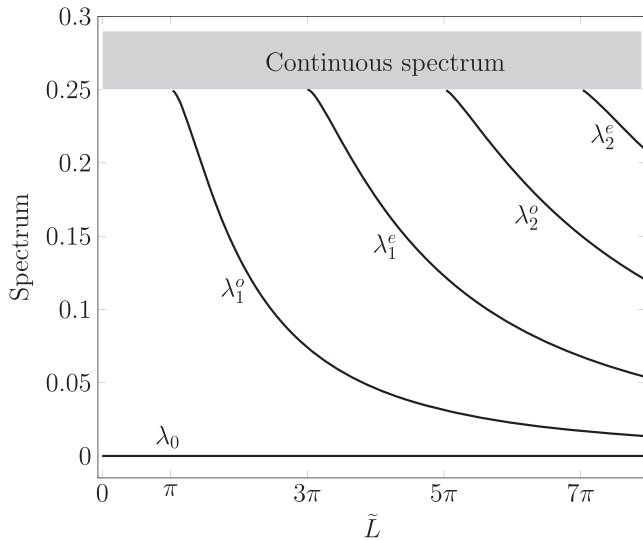


Figure 4. Spectrum of the Fokker–Planck operator as a function of the system size \tilde{L} . The continuous spectrum’s range is $1/4 < \lambda < \infty$, regardless of \tilde{L} . On the other hand, the number of discrete eigenvalues increases with \tilde{L} in a sequence that alternates odd (λ_k^o) and even eigenvalues (λ_k^e). The equilibrium eigenvalue $\lambda_0 = 0$ is always present.

as sketched in figure 4. There is no degeneracy in the discrete spectrum; an eigenvalue cannot solve equations (9) and (10) simultaneously. This allows a strict ordering: $\lambda_0 < \lambda_1^o < \lambda_1^e < \lambda_2^o < \dots$.

Further analysis of equations (9) and (10) yields the large \tilde{L} behavior for the discrete eigenvalues:

$$\lambda_{k \gg 1}^o \sim \frac{4\pi^2}{\tilde{L}^2} \left(k - \frac{1}{2}\right)^2, \quad 1 \leq k \leq N_{\lambda^o}, \quad (13)$$

$$\lambda_{k \gg 1}^e \sim \frac{4\pi^2}{\tilde{L}^2} k^2, \quad 0 \leq k \leq N_{\lambda^e} - 1. \quad (14)$$

This implies that for large colloid separations the relaxation time is quadratic in \tilde{L} , regardless of \tilde{x}_0 . In other words, the large L limit yields, quite expectedly, the same spectrum as a free diffusion in a box of size L .

We conclude with the explicit expression for the relaxation time. For this purpose, we identify the dominant term of equation (5) at large times, which is associated to the minimum nonzero eigenvalue among the non-vanishing projection of the ionic density onto the eigenbasis. This means that, unlike the spectrum, the relaxation time does depend on the ICs. Indeed, there are two distinct behaviors depending on the symmetry of the IC: $\tilde{x}_0 = 0$ (symmetric) and $\tilde{x}_0 \neq 0$ (asymmetric). For the former, we have $\nu_k^o(0) = 0$ and therefore only the even branches in figure 4 do matter in equation (5). Then, the relaxation time is given by

$$\tilde{\tau} = \begin{cases} \max \left\{ 4, \frac{1}{\lambda_1^o} \right\}, & \tilde{x}_0 \neq 0, \\ \max \left\{ 4, \frac{1}{\lambda_1^e} \right\}, & \tilde{x}_0 = 0. \end{cases} \quad (15)$$

2.3. Simulations

This section introduces a method to estimate the relaxation time using the counterion density. The scheme is tested on the exact density and approximation obtained from a computer simulation. Then, these results are compared to the theoretical spectral gap. In this way, the single counter-ion case, which provides us with reference analytic results, is used as a test bench for the method which is later employed for $N > 1$ counterions.

2.3.1. Relaxation time estimation scheme. First, the Kullback–Leibler divergence (KLD) [64] is introduced, as it will be used in the relaxation time estimation scheme. Also known as relative entropy and widely used in information theory, this function is defined as:

$$D_{\text{KL}}(\rho_1 \parallel \rho_2) = \int_{\mathbb{R}} dx \rho_1(x) \log \frac{\rho_1(x)}{\rho_2(x)}, \quad (16)$$

where ρ_1 and ρ_2 are probability densities and $D_{\text{KL}}(\rho_1 \parallel \rho_2)$ is defined as the KLD from ρ_2 to ρ_1 . The discrete definition of the KLD follows from replacing probability densities for probabilities, and performing a summation instead of integrating. The relative entropy is bounded from below $D_{\text{KL}}(\rho_1 \parallel \rho_2) \geq 0$, with equality satisfied when $\rho_1 = \rho_2$, provided that ρ_1 and ρ_2 are both normalized. The KLD is not a metric because it is neither symmetric nor does it obey the triangular inequality. Nonetheless, it is conveniently related to the relaxation time when used with the appropriate distributions: $p(\tilde{x}, \tilde{t} \mid \tilde{x}_0)$ and $p_{\infty}(\tilde{x})$.

For large times, the KLD of the equilibrium distribution p_{∞} to the instantaneous density p decreases exponentially to zero. To see this, consider the ionic density; from (5) it follows that

$$p(\tilde{x}, \tilde{t} \mid \tilde{x}_0) = p_{\infty}(\tilde{x}) + \delta p(\tilde{x}, \tilde{t}, \tilde{x}_0), \quad (17)$$

where $\delta p(\tilde{x}, \tilde{t}, \tilde{x}_0)/p_{\infty}(\tilde{x}) \ll 1$ at long times. Then, the KLD from p_{∞} to p has the following large time behavior:

$$\begin{aligned} D_{\text{KL}}(p \parallel p_{\infty}) &\sim \int_{\mathbb{R}} \delta p d\tilde{x} + \int_{\mathbb{R}} \frac{(\delta p)^2}{p_{\infty}} d\tilde{x} + \mathcal{O} \left((\delta p/p_{\infty})^2 \right) \\ &\sim \int_{\mathbb{R}} \frac{(\delta p)^2}{p_{\infty}} d\tilde{x} + \mathcal{O} \left((\delta p/p_{\infty})^2 \right), \end{aligned} \quad (18)$$

where the integral of δp vanishes in view of equation (17) and the fact that both p and p_{∞} are normalized. Likewise, the associated divergence with transposed arguments ($D_{\text{KL}}(p_{\infty} \parallel p)$) exhibits the same asymptotic behavior as that given by equation (18). From equation (18) we observe that the KLD has an exponential decay constant $2/\tilde{\tau}$, which is twice the value for the ionic density itself.

The term $(\delta p)^2$ induces two distinct behaviors for $D_{\text{KL}}(p \parallel p_{\infty})$ depending on the symmetry of the IC: $\tilde{x}_0 = 0$ (symmetric) or $\tilde{x}_0 \neq 0$ (asymmetric). In the former case, the projection of the ionic density onto odd eigenfunctions vanishes and therefore only the even branches of the spectrum in figure 4 do matter. We next describe the asymmetric case, which in

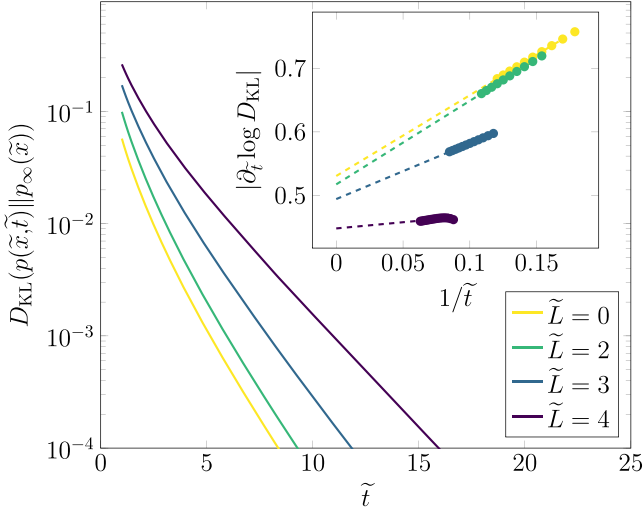


Figure 5. KLD for one counterion $N = 1$ with various colloid separations $\tilde{L} = 0, 2, 3, 4$ and initial counterion position $\tilde{x}_0 = \tilde{L}/4$. Note that for $\tilde{L} < \pi$, the log KLD is still convex-up for $D_{\text{KL}} > 10^{-4}$ due to the subdominant power law \tilde{t}^{-s} in equation (19). Contrarily, for $\tilde{L} > \pi$ the curvature vanishes quickly since the subdominant term decreases exponentially. The inset is a sketch of the scheme to estimate the relaxation time $\tilde{\tau}$ for a given \tilde{L} . Each same color set of points is the numerical derivative of the logarithm of $D_{\text{KL}}(p(\tilde{x}, \tilde{t} | \tilde{x}_0) || p_\infty(\tilde{x}))$ as a function of the inverse time. The dashed lines are the corresponding minimum square regressions, used to extrapolate the behavior of the dots to $1/\tilde{t} = 0$. According to equation (19), this yields twice the decay rate, $2/\tilde{\tau}$.

appendix C is found to be:

$$D_{\text{KL}}(p || p_\infty) \sim \begin{cases} \tilde{t}^{-s} e^{-2\tilde{t}/4} = \tilde{t}^{-s} e^{-2\tilde{t}/\tilde{\tau}}, & \tilde{L} < \pi \\ e^{-2\tilde{t}/\lambda_1^0} = e^{-2\tilde{t}/\tilde{\tau}}, & \tilde{L} > \pi, \end{cases} \quad (19)$$

where $1/2 < s < 5/2$. Although for very large times the algebraic term \tilde{t}^{-s} is negligible, this is not the case for the times available in the simulations, which may cause a difficulty in extracting the decay rate. Take for example the case $\tilde{x}_0 = \tilde{L}/4$ (figure 5): notice the curve's concavity for $\tilde{L} < \pi$, which stems from the subleading term of order $\log \tilde{t}$ in the logarithm of the KLD. On the contrary, for $\tilde{L} > \pi$ this term is always negligible. The symmetric case $\tilde{x}_0 = 0$ is similar to equation (19), provided the substitutions $\lambda_1^0 \rightarrow \lambda_1^e$ and $\pi \rightarrow 3\pi$ are performed. The inset of figure 5 presents the method used for extracting the decay rate τ from the dynamical data.

2.3.2. Numerical integration. We now proceed to introduce the simulation used to compute the numeric density profiles. We integrate the following stochastic Langevin equation

$$\dot{\tilde{x}} = \tilde{F}(\tilde{x}, \tilde{L}) + \xi(\tilde{t}), \quad (20)$$

where $\tilde{F}(\tilde{L}) = -\partial\tilde{\Phi}/\partial\tilde{x}$ is the dimensionless force. Equation (20) is equation (2) in rescaled units. We record 10^8 positions per time. Each temporal step was set to 4×10^{-4} and a histogram was recorded every 200 time steps, using bins of size 0.2. These histograms give the numeric estimation of the ionic density, $p(\tilde{x}, \tilde{t})$.

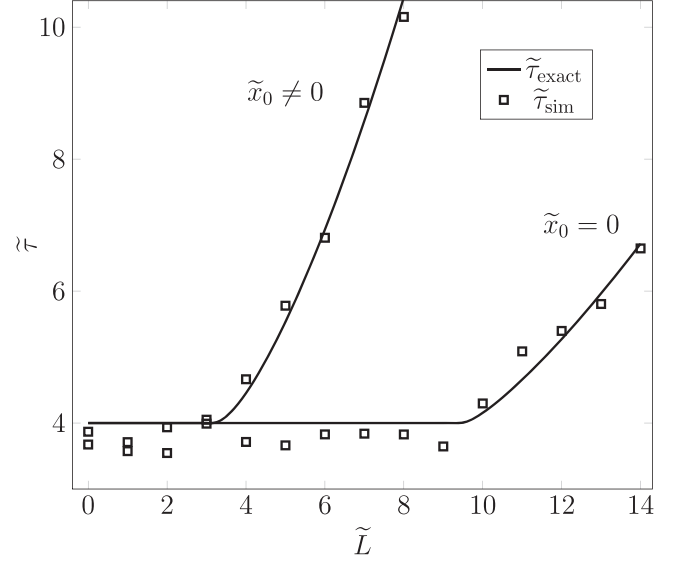


Figure 6. Relaxation time for a system made of two colloidal particles at a distance \tilde{L} and one counterion ($N = 1$), from the exact calculation (solid) given by equation (15) and an estimation using a simulation (squares). Two cases for the localized initial distribution should be distinguished: asymmetric ($\tilde{x}_0 \neq 0$) and symmetric ($\tilde{x}_0 = 0$).

Then, the discrete KLD $D_{\text{KL}}(p(\tilde{x}, \tilde{t}) || p_\infty(\tilde{x}))$ is calculated. The relaxation times follow from the long-time behavior of D_{KL} , as explained above; the results are shown in figure 6, where the numerical scheme is seen to be in agreement with the analytical curve. Finally, note that the relaxation time $\tilde{\tau}_{\text{sim}}$ extracted from the simulations for a symmetric IC (SIC) exhibits a slight non-monotonous behavior in the vicinity of $\tilde{L} = 9$. This non-monotonicity appears to be an artifact of the numerical procedure used. We come back to this in section 3.

We conclude with some additional remarks on our numerical study. It is based on simulations of the Brownian dynamics that describe the time evolution of the system. For our purposes, the Euler–Maruyama method [65] is both the simplest and most efficient technique to simulate the counterions' paths. The reason for this is that the coefficients of the white noise terms in the Langevin equations (defining the diffusion coefficients) are all constant in time and the electrostatic force is bounded; these are sufficient conditions for numerical convergence of weak order 1.0 [66, 67]. Higher-order methods do not provide any computational advantages, as they usually rely on derivatives of the white noise term coefficients [68], so the only real improvement in this direction is the use of computation in parallel. As it is necessary to collect n samples to obtain results with a precision of order $n^{-1/2}$ from simulations, computation in parallel provides a way to obtain results with high precision at a reasonable computation cost.

2.4. First passage time

At equilibrium, the counterion plays an important role in the pressure: the colloids share this particle, which for large

enough \tilde{L} , induces them to attract each other [51]. It is of interest to investigate how the counterion is shared, and how much time it spends in the vicinity of one colloid before reaching the other.

The first passage time \tilde{T} , with initial and final position on each colloid, is an appropriate quantity to measure the crossing time between colloids. Due to the symmetry of the system we can choose the particle starting on either side and ending in the opposite side. Taking the initial position of the counterion to be at the left colloid $-\tilde{L}/2$ and the final position at the right colloid $\tilde{L}/2$, the first passage time distribution $w_{\tilde{L}}(\tilde{T})$ follows from:

$$w_{\tilde{L}}(\tilde{T}) = - \int_{-\infty}^{\tilde{L}/2} \frac{\partial}{\partial \tilde{T}} P_a(\tilde{x}, \tilde{T} | -\tilde{L}/2) d\tilde{x}, \quad (21)$$

where $P_a(\tilde{x}, \tilde{T} | \tilde{x}_0)$ is the probability density function of an initially localized counterion at \tilde{x}_0 with an absorbing wall at $\tilde{L}/2$ (see [62]). Since P_a follows from solving equation (3) with different boundary conditions than those for p (equation (5)), the Fokker–Planck operator for P_a features a different spectrum. It has both a continuous and a discrete part, and their boundaries are: $\lambda^a \in (1/4, \infty)$ and $0 < \lambda_k^a < 1/4$ respectively. The discrete part of the spectrum follows from solving

$$1 - \sqrt{1 - 4\lambda_k^a} = 2\sqrt{\lambda_k^a} \cot(\sqrt{\lambda_k^a} \tilde{L}), \quad (22)$$

which has no solutions for $\tilde{L} < \pi/2$. Therefore, the spectrum is completely continuous when $\tilde{L} < \pi/2$, leaving aside the gapped steady-state eigenvalue $\lambda = 0$.

In a similar fashion as for P , we obtain the analytic solution for P_a and consequently for the first passage time distribution $w_{\tilde{L}}(\tilde{T})$:

$$w_{\tilde{L}}(\tilde{T}) = \int_{1/4}^{\infty} e^{-\lambda^a \tilde{T}} \frac{\sqrt{4\lambda^a - 1} \sin(\sqrt{\lambda^a} \tilde{L})}{2\pi\sqrt{\lambda^a} - \pi \sin(2\sqrt{\lambda^a} \tilde{L})} d\lambda^a + \sum_k \frac{e^{-\lambda_k^a \tilde{T}} \left[1 + 2\sqrt{\lambda_k^a} \tan\left(\frac{\sqrt{\lambda_k^a} \tilde{L}}{2}\right) - \sqrt{1 - 4\lambda_k^a} \right]}{2(1 - 4\lambda_k^a)^{-1/2} + \tilde{L} \csc^2(\sqrt{\lambda_k^a} \tilde{L}) - \cot(\sqrt{\lambda_k^a} \tilde{L}) / \sqrt{\lambda_k^a}} \quad (23)$$

where $\lambda_k^a < 1/4$ is a solution of equation (22). From the spectrum follows the asymptotic behavior which decays as $e^{-\tilde{T}/4}$ for $\tilde{L} < \pi/2$ and as $e^{-\lambda_1^a \tilde{T}}$ for $\tilde{L} > \pi/2$ where λ_1^a is the smallest discrete eigenvalue.

The previous behavior bears a resemblance to the first passage time distribution of a free diffusing particle in a box of length \tilde{L} . This situation consists of a free Brownian motion $\tilde{X}(\tilde{t})$ with diffusion constant equal to one and started at the origin. We place a pair of fixed walls, a reflecting one at the origin and an absorbing one at a distance $l > 0$. Then, we define the transport time as the first hitting time of \tilde{l} , that is,

$$\tau_{\tilde{l}} = \inf\{\tilde{t} > 0 : \tilde{X}(\tilde{t}) \geq \tilde{l}\}. \quad (24)$$

We derive the distribution $q_{\tilde{l}}(\tilde{t})$ of $\tau_{\tilde{l}}$ in appendix D:

$$q_{\tilde{l}}(\tilde{t}) = \sum_{n=0}^{\infty} (-1)^n \frac{\pi (2n+1)}{\tilde{l}^2} \exp\left(-\frac{\pi^2(2n+1)^2}{4\tilde{l}^2} \tilde{t}\right). \quad (25)$$

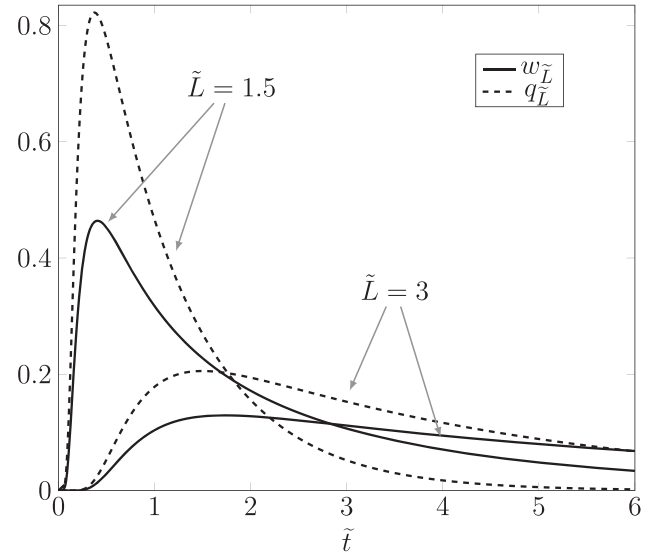


Figure 7. First passage distribution for a single counter-ion traveling between the colloids ($w_{\tilde{L}}$, solid) and a free diffusing particle in a box ($q_{\tilde{L}}$, dashed) with a colloid/box length of $\tilde{L} = 1.5$ and 3. The former is seen to have a larger mean first passage time and variance: in that case the counter-ion has the possibility to make excursions with $\tilde{x} < 0$ outside the region delimited by the colloids unlike the box situation where it is limited to a finite space.

The confined Brownian particle exhibits a smaller average first passage time and variance than the one counter-ion colloid (see figure 7). This is expected since it does not have an infinite region available to wander off. In the following section the boxed particle model will allow us to understand the behavior of the crossing time of the M th particle when $N = 2M - 1$ (the middle/misfit counter-ion), from one colloid double-layer to another. In this sense, the case $N = 1$ is different from all the odd $N > 1$ where the colloids have screening particles that prevent the middle counter-ion from scouting the exterior regions. In fact, we will see that the effective length l is smaller than L .

3. Relaxation time for multiple counterions

We move on to describe the relaxation time for the multiple counterion case, $N > 1$. Each counterion has fixed charge e , and the colloid charge $-Ne/2$ ensures electroneutrality. An analytical or numerical solution of the Fokker–Planck equation is impractical since it involves a partial differential equation in $N + 1$ dimensions. Instead, we perform simulations of the corresponding Langevin equation to compute the time evolution of the density profile $n(\tilde{x}, \tilde{t}; N)$. To obtain the relaxation time, we analyze the evolution of the KLD between the density at time \tilde{t} and the equilibrium one by extending the scheme introduced in section 2.3. This is done by replacing the single particle counterion density with the normalized counterion density profile n/N . This normalization is necessary to use the KLD, which is defined for probability density functions. Besides from the time evolution, we require the equilibrium density profile $n_{\infty}(\tilde{x}; N)$, which has the following analytical

expression:

$$n_\infty = \sum_{N_\ell=0}^N \sum_{N_r=0}^{N-N_\ell} \frac{z_{N_\ell, N_r}(N, \tilde{L})}{Z(N, \tilde{L})} n_{N_\ell, N_r} \left(\tilde{x} + \frac{\tilde{L}}{2}, N, \tilde{L} \right), \quad (26)$$

where $Z(N, \tilde{L}) = \sum_{N_\ell=0}^N \sum_{N_r=0}^{N-N_\ell} z_{N_\ell, N_r}(N, \tilde{L})$. The functions $z_{N_\ell, N_r}(N, \tilde{L})$ refer to partition functions of a system with a fixed number of particles at the left (N_ℓ) and right (N_r) sides and are given in [52] (equations (52)–(55)), and n_{N_ℓ, N_r} are the density functions with fixed number of particles at each side and are given by equations (59)–(61) of reference [52]. Those results are for a system of two symmetric impermeable colloids and N counterions distributed in the three possible regions: N_ℓ , N_r and $N - N_\ell - N_r$ are in the regions $x < 0$, $\tilde{x} > \tilde{L}$ and $0 < \tilde{x} < \tilde{L}$ respectively. These results must be translated to coincide with the present situation $\tilde{x} \rightarrow \tilde{x} + \tilde{L}/2$, and then the sum over all the possible impermeable configurations weighted by $z_{N_\ell, N_r}(N, \tilde{L})/Z(N, \tilde{L})$ yields the permeable result.

The time evolution of the density profile $n(\tilde{x}, \tilde{t}; N)$ is computed using a numerical simulation of the Langevin equation. The advantage of this scheme is that it is easily extended to an N counter-ion system. The system of Langevin equations to be simulated is

$$\dot{\tilde{x}}_j = \tilde{F}_j(\tilde{x}_1, \dots, \tilde{x}_N) + \xi_j(\tilde{t}), \quad (27)$$

where $\langle \xi_i(\tilde{t}') \xi_j(\tilde{t}) \rangle = 2\delta_{ij} \delta(\tilde{t} - \tilde{t}')$, $\langle \xi_i(\tilde{t}) \rangle = 0$ and $\tilde{F}_j = F_j \epsilon kT / e^4$ is the dimensionless Coulomb force on the particle at \tilde{x}_j :

$$\begin{aligned} \tilde{F}_j(\tilde{x}_1, \dots, \tilde{x}_N) = & \sum_{\substack{i=1 \\ i \neq j}}^N \text{sgn}(\tilde{x}_j - \tilde{x}_i) - \frac{N}{2} \text{sgn} \left(\tilde{x}_j + \frac{\tilde{L}}{2} \right) \\ & - \frac{N}{2} \text{sgn} \left(\tilde{x}_j - \frac{\tilde{L}}{2} \right), \end{aligned} \quad (28)$$

where $\text{sgn}(x)$ is the sign function. Equation (27) with a force given by equation (28) is very close to a one-dimensional Brownian particle system with rank-dependent drifts [69], with the difference that the fixed colloids disable the rank-dependence because the drift of the counterion also depends on its position relative to the fixed points $-\tilde{L}/2$ and $\tilde{L}/2$. With these two ingredients, we can compute $D_{\text{KL}}(p(\tilde{x}, \tilde{t}; N) \| p_\infty(\tilde{x}; N))$, where $p(\tilde{x}, \tilde{t}; N) = n(\tilde{x}, \tilde{t}; N)/N$ is the normalized density profile and $p_\infty(\tilde{x}; N)$ the corresponding equilibrium state (equation (26)).

The simulations for the many counterions case use the same time and position discretization as for $N = 1$. The number of positions recorded per particle is of order 10^7 . For $N = 1$, a SIC annihilates the projection of the ionic density onto the first non-zero eigenvalue (λ_1^0), and therefore changes the relaxation time. In view of this phenomenon, we implement two IC with

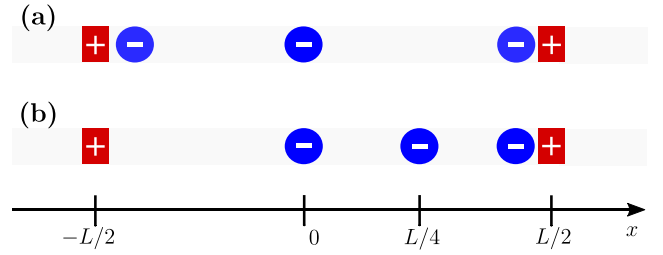


Figure 8. Sketch of ICs (equation (29)) used for the colloid simulation (here $N = 3$): (a) SIC and (b) AIC.

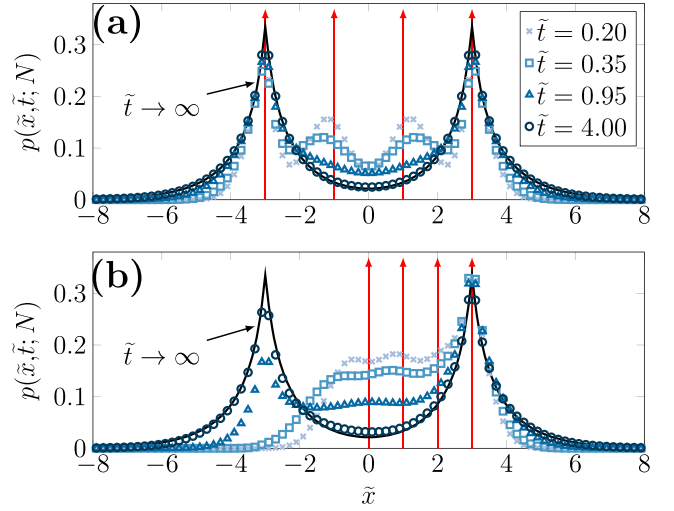


Figure 9. Time evolution of the normalized density profile $p(\tilde{x}, \tilde{t}; N)$ for $N = 4$ counterions and colloids at distance $\tilde{L} = 6$. The red arrows represent the localized ICs: (a) symmetric and (b) asymmetric. The solid line is the exact equilibrium distribution. Note that for $\tilde{t} \approx 4$ the density has almost reached its steady state.

different parity, as presented in figure 8 and specified by

$$\begin{aligned} \text{Symmetric IC} &= \left\{ -\frac{\tilde{L}}{2}, \dots, \frac{(2k-1-N)\tilde{L}}{2(N-1)}, \dots, \frac{\tilde{L}}{2} \right\} \\ \text{Asymmetric IC} &= \left\{ 0, \dots, \frac{(k-1)\tilde{L}}{2(N-1)}, \dots, \frac{\tilde{L}}{2} \right\}, \end{aligned} \quad (29)$$

where $k \in \{1, \dots, N\}$.

The dynamics in the many counterion case is determined by two parameters: colloid separation and number of counterions. However, there are a few general properties that we proceed to describe using a concrete example: $N = 4$ and $\tilde{L} = 6$ which is plotted in figure 9. As a consistency check, note that the simulation approaches the exact equilibrium result (solid line). From $p_\infty(\tilde{x}; N)$ we know that the first moment vanishes at infinite times, which is readily seen from the figure 9 at $\tilde{t} \approx 4$. The position variance is seen to be monotonic as the density profile expands to its equilibrium state, just as for $N = 1$ with the counterion initially in the region between the colloids. Both the first moment and the variance decay exponentially to their respective terminal values. The following part of the paper moves on to describe this process.

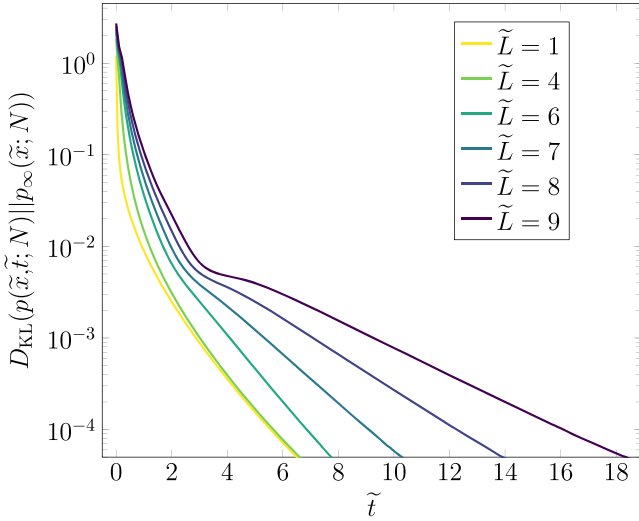


Figure 10. Numeric KLD for $N = 15$ in the AIC case. Note the strong positive concavity for $\tilde{L} = 4$ in the vertical range between 10^{-3} and 10^{-4} .

3.1. Odd number of counterions

Let us begin this part with the asymmetric IC (AIC) case. Figure 10 shows the time evolution of the KLD obtained from simulations with $N = 15$ counterions. In order to carry out the extrapolation scheme described in section 2.3.1, we take the data points where the KLD lies between 10^{-3} and 10^{-4} . It is clear from figure 10 that the log KLDs for $1 \leq \tilde{L} \leq 4$ are convex-up in this region, but no concavity is visible for $\tilde{L} \geq 6$. In the following discussion, it will appear that the behavior for odd $N > 1$ can be mapped onto the $N = 1$ case; the middle particle indeed acts as for $N = 1$, but in a reduced length: the whole colloid–colloid length L is no longer accessible, given the presence of the ions localized in the vicinity of the colloids. An effective length, L minus the two double-layer sizes, turns out to make the above mapping operational. We come back to this question in section 5. In the one-counterion case with AIC, the first nonzero discrete eigenvalue appears when $\tilde{L} \geq \pi$ according to equation (11); in the present situation with $N > 1$, taking into account the double-layer size of the ion clouds, we may surmise that this eigenvalue appears at a slightly larger \tilde{L} . Indeed, this is confirmed in figure 11, where the characteristic time seems to be close to $\tilde{\tau} = 4$ for $\tilde{L} \leq 4$, and increases for $\tilde{L} \geq 6$.

When imposing the SIC, the projection of p onto any odd eigenfunction vanishes. Therefore, the dominating term becomes λ_1^e , which for $N = 1$ separates from the continuum at $\tilde{L} \geq 3\pi$, according to equation (12). If we take the double-layer size into account, we expect the separation of this eigenvalue to occur at around $\tilde{L} = 10$. The corresponding dynamics of the KLDs for $N = 15$ are very similar in shape to those shown in figure 10, in that the log KLDs show a noticeable convex behavior in the range between 10^{-3} and 10^{-4} for small \tilde{L} . This convexity disappears for large \tilde{L} , a phenomenon that seems to occur at $\tilde{L} > 10$, and that is reflected in figure 11. As expected from our considerations in the single counterion

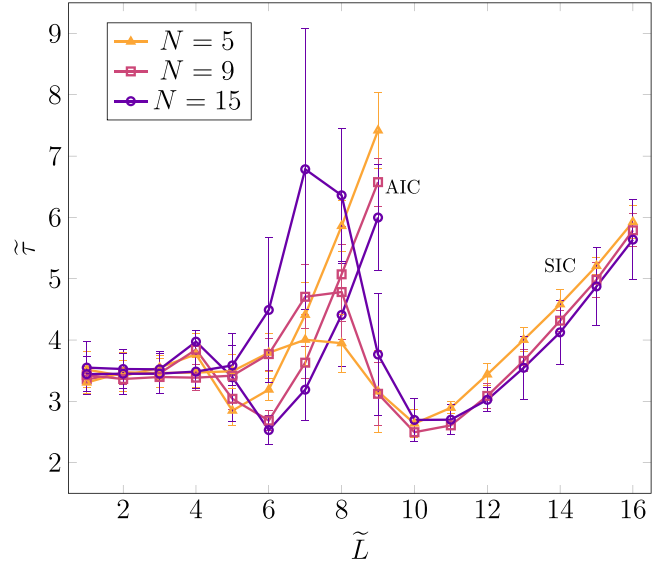


Figure 11. Numerical estimation of the relaxation time $\tilde{\tau}$ as a function of \tilde{L} for $N = 5, 9, 15$ with AIC and SIC initial conditions (equation (29)). The straight lines are guides to the eye. Note the overall resemblance with the case $N = 1$ (figure (6)): a constant region at short colloid separations is followed by a quadratic increase of $\tilde{\tau} \sim \tilde{L}^2$ at large \tilde{L} . The error bars denote one standard deviation, obtained from the spread in the linear fits outlined in section 2.3.1 performed over a moving window of 30 consecutive data points.

case, we observe that the characteristic time is compatible with $\tilde{\tau} \simeq 4$ for $\tilde{L} \leq 6$, and that it increases for $\tilde{L} > 10$.

While the diffusive behavior of the relaxation time for N odd is due to the misfit, one may wonder how fast all other ions do relax, and surmise that they presumably do so on a much smaller time scale than $\tilde{\tau}$. We show now that this indeed is the case and examine the effect of the middle particle in the double-layer relaxation. To this end, we have considered the density of the counterions discarding the misfit, and investigated how it departs from its equilibrium distribution, through the corresponding KLD. In figure 12, the resulting dashed curve, for $N = 15$, does not exhibit a pure exponential behavior, but its slope yields a relaxation time close to 1.3, which is significantly smaller than the $\tilde{\tau}$ value, here close to 6.0, and given by the large time slope of the continuous $N = 15$ curve. For completeness, we also report a benchmark calculation for $N = 14$. There is then no misfit, but this calculation allows to estimate the effect of removing ions for the KLD considered. We note that the two curves for $N = 14$ quickly become parallel, and thus yield the same decay rate. This is at variance with the situation at $N = 15$. In the following section, the case where N is even is explored in detail.

3.2. Even number of counterions

We now consider an even number of counterions. For this case we do not possess any analytical results. However, we expect that for two counterions ($N = 2$) and $\tilde{L} \gg 1$, there is correspondence to the system with a single counterion ($N = 1$) and zero colloid separation ($\tilde{L} = 0$). The rationale behind this argument is that at large colloid separations, the N counterions split

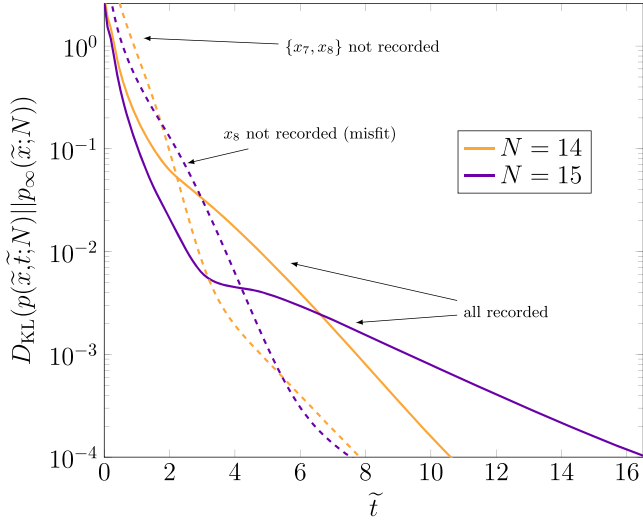


Figure 12. KLD of a modified ionic density (dashed) at a given time and its equilibrium distribution, for $\tilde{L} = 9$. For $N = 15$, the simulation does not record the misfit’s position (x_8). Likewise, for $N = 14$ the middle particles x_7, x_8 are not recorded. The solid curves correspond to the case where the true counterion density profile is used.

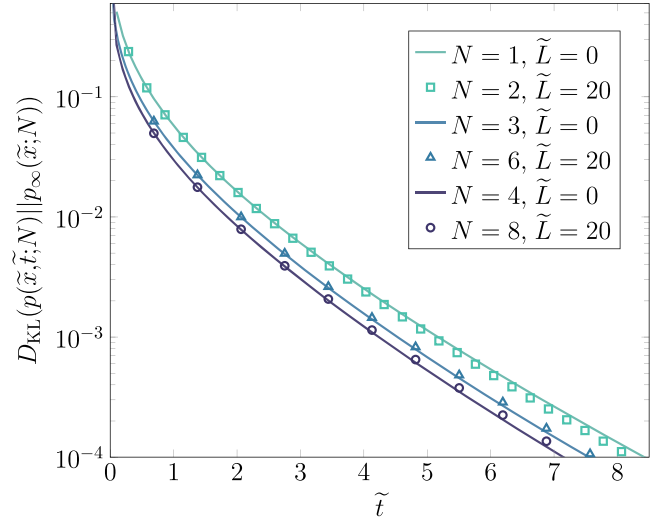


Figure 13. KLD for one counter-ion (analytic) and for $N = 2, 3, 4, 8$ counter-ions (numerical). Solid lines have $\tilde{L} = 0$ and marks $\tilde{L} = 20$ (large colloid separation). Data for $N/2$ and N counterions do overlap. The agreement of each pair of curves shows that at large distances, a system with even N counterions effectively behaves as two decoupled neutral subsystems of $N/2$ counterions.

into two groups of $N/2$ particles which completely screen each colloid. In other words, two neutral subsystems are formed. Moreover, the screened colloids do not exert any force onto each other. Hence, there is an effective decoupling of the whole system into two non-interacting screened colloids, with $N/2$ counterions each. Consequently, we expect the case $N = 1$ and $\tilde{L} = 0$ to have the same relaxation toward equilibrium as $N = 2$ and large \tilde{L} . In figure 13, we see that both systems share the same KLD. Note that the mapping $(N, \tilde{L} \gg 1) \rightarrow (N/2, \tilde{L} = 0)$ holds for any even N , as seen in figure 13 for a couple of cases ($N = 2, 6, 8$).

Figure 14 shows the simulation based estimation for the relaxation time as a function of \tilde{L} , for several even N . The results for $N \geq 2$ give evidence that the relaxation time has constant value $\tilde{\tau} = 4$ for any \tilde{L} . This is seen for both ICs (equation (29)) and suggests that $\tilde{\tau}$ is independent of both N and \tilde{L} . Additionally, physical arguments lead to the same conclusion in limiting cases, such as the aforementioned mapping $(N, \tilde{L} \gg 1) \rightarrow (N/2, \tilde{L} = 0)$. In figures 11 and 14 we observe that for every N considered, the relaxation time is $\tilde{\tau} = 4$ when the colloids are together ($\tilde{L} = 0$). Therefore, it is plausible that when N is even and the colloids are sufficiently separated, the relaxation time is also 4.

An argument to understand the \tilde{L} independence phenomenon goes as follows: for even N , the left and right moieties of the system, each being neutral, are decoupled. The only L dependence in the problem therefore arises through the IC, that does not affect the relaxation rate measured. Of course, ICs with counterions more distant from their native colloid will collectively take longer to relax than if all ions would start, say, from a typical equilibrium double-layer distance from the colloid. Yet, this difference will manifest itself in the short time evolution, and leave unaffected the large-time decay rate. Indeed, ions starting far away from their native

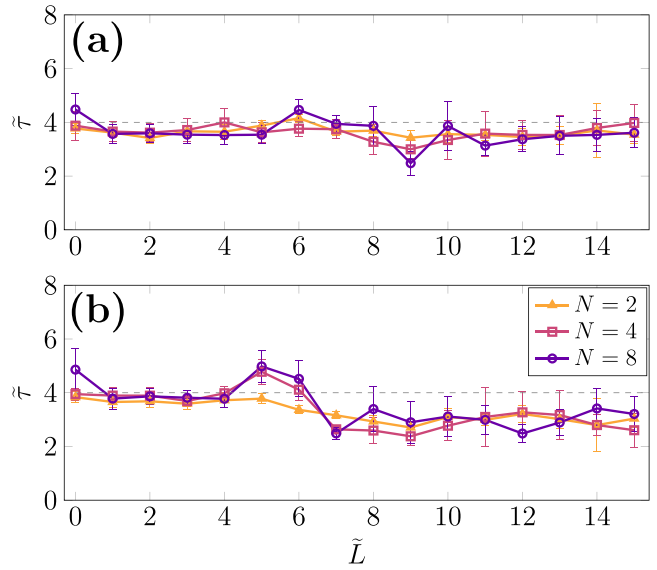


Figure 14. Relaxation time $\tilde{\tau}$ estimation for $N = 2, 4, 8$ counterions as a function of colloid distance \tilde{L} for two ICs (equation (29)): (a) symmetric and (b) asymmetric. The straight lines are guides to the eye.

colloid will undergo a ballistic motion on average. Such behavior occurs in a finite time, whereas the equilibration of the double-layer is an exponential decay. The N independence is traced to the double-layer’s length, which is practically constant in N when expressed in units of l_B , as done here [51]. Then, for any number of counterions, the space to be probed is the same.

Our results are limited by the minimum value obtained for D_{KL} , which is mainly determined by the binning of positions used to compute the histograms at each time. As \tilde{t} increases,

so does the number of simulations needed. This especially affects the AIC that requires a larger \tilde{t} to be in the regime where $\log D_{\text{KL}}$ is ruled by a linear term in time and with a subdominant (yet relevant) term $\log \tilde{t}$. In that regime the method for determining the relaxation time is very effective, as previously seen in N odd and for the analytic solution when $N = 1$.

To summarize, two essentially different scenarios are identified depending on the parity of N . The odd N case has a qualitative behavior identical to the single counter-ion case. When $\tilde{L} < \tilde{L}^*(N)$ then $\tilde{\tau} = 4$, where $\tilde{L}^*(N) \geq \pi$ is some length dependent on N . For large \tilde{L} the relaxation time is quadratic on the distance: $\tilde{\tau} \propto \tilde{L}^2$, showing typical diffusive behavior. On the other hand, when N is even, we gave evidence that the relaxation time is both N - and \tilde{L} -independent. In all cases, the relaxation dynamics follow the exponential decay outlined in equation (19), which is fundamentally different from the long-time behavior shown by similar systems with weak-coupling, that are amenable to a mean-field treatment. We now establish the connection between these two behaviors.

4. Mean-field dynamics

In this section, we consider the dynamics within a mean-field treatment. This approach is justified in the weak-coupling regime; in our case, this corresponds to taking the limit $e \rightarrow 0$ and $N \rightarrow \infty$ while keeping Ne fixed (i.e. the colloids charge). This was shown analytically using different formulations in [50, 51], for an equilibrium system with counterions limited to remain in the inter-colloidal space. We generalize here to the dynamics.

To keep the discussion within reasonable bounds, we focus on the case $L = 0$, which can alternatively be seen as a single colloid with charge $2Q$. Yet, we expect the general conclusions to extend to $L \neq 0$. The mean-field problem then admits a simple exact solution, be it at equilibrium or out of equilibrium, that allows to draw conclusions from analytic expressions and to assess how a discrete system approaches the mean-field regime. We will now treat the counterions as a continuous charge distribution rather than a discrete set of point-particles. We consider a system made of two colloids at the origin, each of charge Qe , together with the counterion distribution. The top illustration in figure 15 envisions the mean-field system, were we take the distance between colloids to be zero. Although our discussion is centered in a 1D Coulomb gas, the mean-field results in this section also describe systems in 2D and 3D, as depicted in figure 15. Since our system is symmetric with respect to the origin, we restrict to $x > 0$. First, we analyze the equilibrium behavior, which follows from solving the Poisson–Boltzmann (PB) equation [70]:

$$\phi_{\text{PB}}''(x) = \frac{2n_0e}{\epsilon} \exp\{e\beta\phi_{\text{PB}}(x)\}, \quad (30)$$

where n_0 is a normalization constant. The previous equation is complemented with the boundary condition $\phi_{\text{PB}}'(0^+) = -2Qe/\epsilon$, which accounts for the colloidal charge. Equation (30) is obtained by assuming the counterions

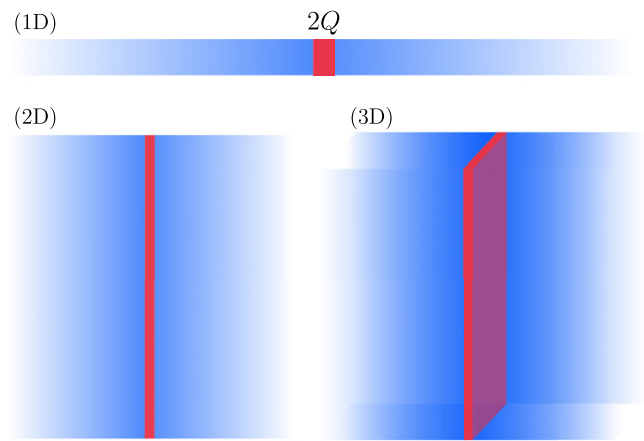


Figure 15. Sketch for three mean-field systems described by the same equation: a point charge in 1D (top), a uniformly charged line in 2D (bottom left) and a uniformly charged plate in 3D (bottom right). In red are the colloids (point/line/plate) and in blue the counterions which have a continuous charge distribution. At equilibrium, exactly half of the distribution lies within a Gouy–Chapman length from its colloid. Under the appropriate time and length rescaling, the equations in (PB) and out of equilibrium (PNP) are identical for these three systems. In 1D, this system is the mean-field counterpart of the point-particle case envisioned by figure 1, at $L = 0$.

have a Boltzmann distribution $n_0 \exp(-e\beta\phi_{\text{PB}})$ and then inserting this density into Poisson equation. The solution to equation (30) is

$$n_{\text{PB}}(x) = \frac{Q}{b(1+x/b)^2}, \quad (31)$$

where $b = \epsilon/\beta Qe^2$ is the Gouy–Chapman length. In 1D, this quantity is proportional to the Bjerrum length $b = l_B/Q$.

In order to discuss the mean-field results, we rescale the position by the b length: $\hat{x} = x/b$ and introduce the reduced density $\hat{n} = (b/Q)n$. Figure 16 features the PB density and three exact profiles for $N = 1, 5$ and 20 , computed using equation (26). The plot shows that by increasing N , the discrete result approaches the PB density. Beyond a few particles (e.g. 5), the effect of increasing N mostly affects the tail behavior.

We now turn to the mean-field dynamics. For this purpose, we solve the dynamical generalization of the PB equation, the Poisson–Nernst–Planck (PNP) equations [1]:

$$\begin{aligned} -\partial_x^2 \phi_{\text{PNP}} &= -2en_{\text{PNP}}/\epsilon, \\ \partial_t n_{\text{PNP}} &= D \partial_x^2 n_{\text{PNP}} - \mu \partial_x (n_{\text{PNP}} \partial_x \phi_{\text{PNP}}), \end{aligned} \quad (32)$$

where D is the diffusion constant and μ the electric mobility of the counterions. These constants are related by the Einstein relation $D = (\mu/e)k_B T_{\text{bath}}$. Again, we account for the colloidal particle by fixing the electric field at the origin for all times:

$$\partial_x \phi_{\text{PNP}}(0^+, t) = -2Qe/\epsilon. \quad (33)$$

We proceed to use the ‘hat’ rescaling, which was already defined for position and ionic density. The remaining time and potential units are given by $\hat{t} = t/(b^2/D)$ and $\hat{\phi}_{\text{PNP}} = e\beta\phi_{\text{PNP}}$

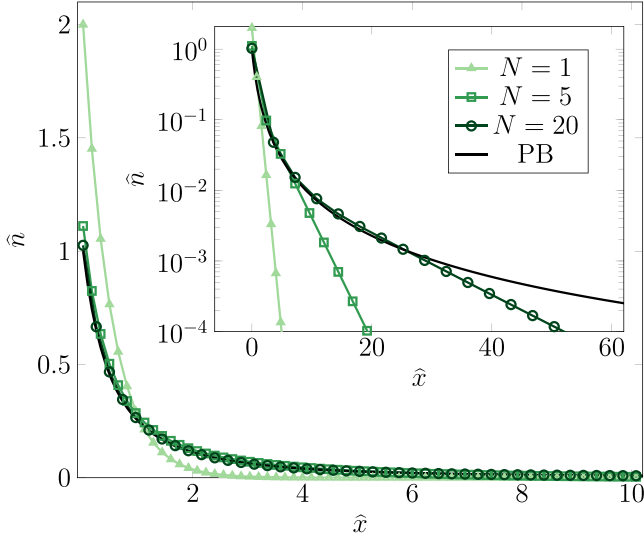


Figure 16. Equilibrium density profile $\hat{n}_\infty(\hat{x})$ (equation (26)) with $L = 0$ for $N = 1, 5, 20$. The solid line is for the PB solution \hat{n}_{PB} . Note that for as few as $N = 5$ counterions, the mean-field theory (i.e. \hat{n}_{PB}) is a good approximation, except in the tail. The inset shows the same plot in logarithmic scale to emphasize the tails: increasing N (while keeping Ne fixed) augments the region of overlap between the discrete and mean-field models.

respectively. In [38] it was shown that integrating twice the second equality in equation (32) and assuming a symmetric initial condition, the electrokinetic equations become

$$\partial_{\hat{t}} \hat{\phi}_{PNP}(\infty, \hat{t}) - \partial_{\hat{t}} \hat{\phi}_{PNP}(\hat{x}, \hat{t}) = \partial_{\hat{x}}^2 \hat{\phi}_{PNP}(\hat{x}, \hat{t}) + \frac{[\partial_{\hat{x}} \hat{\phi}_{PNP}(\hat{x}, \hat{t})]^2}{2} \quad (34)$$

In [38] a Cole–Hopf transformation was used. It amounts to introducing W such that:

$$\hat{\phi}_{PNP}(\hat{x}, \hat{t}) - \hat{\phi}_{PNP}(\infty, \hat{t}) = -2 \ln W(\hat{x}, \hat{t}), \quad (35)$$

which brings interesting simplifications, see below. Note that up to a constant, we have $\hat{\phi}_{PNP}(\hat{x}, \hat{t} \rightarrow \infty) = \hat{\phi}_{PB}(\hat{x}) = 2 \ln(1 + \hat{x})$. As a result, $\hat{\phi}_{PNP}(\infty, \hat{t})$ is divergent for $\hat{t} \rightarrow \infty$. This nevertheless does not lead to any physical difficulty nor any ill-posedness in (35): an additive x -independent term in the potential $\hat{\phi}_{PNP}$ does not change the charge density. What we may gather from the above remark is that

$$\lim_{\hat{x} \rightarrow \infty} W(\hat{x}, \hat{t}) = 1 \quad \text{while} \quad \lim_{\hat{t} \rightarrow \infty} W(\hat{x}, \hat{t}) = 0. \quad (36)$$

We then substitute the Cole–Hopf transformation into equation (34), and it doing so it becomes

$$\partial_{\hat{t}} W = \partial_{\hat{x}}^2 W, \quad (37)$$

which is equipped with the following Robin boundary condition:

$$\partial_{\hat{x}} W(0^+, \hat{t}) - W(0^+, \hat{t}) = 0, \quad (38)$$

as follows from equation (33).

In order to find W , we can use the reflection method where we introduce a function W_0 , defined from a modification of the

IC $W(\hat{x}, 0)$. The idea is to restrict to $\hat{x} \geq 0$, and to continualize W to $\hat{x} < 0$ in a convenient fashion. In order to satisfy the Robin boundary condition, the function W_0 is taken such that $\partial_{\hat{x}} W_0(\hat{x}) - W_0(\hat{x})$ is an odd function, and consequently vanishes at the origin. We also require W_0 to coincide the IC for $\hat{x} > 0$. The function that satisfies the previous requirements is given by:

$$W_0(\hat{x} < 0) = W_0(0)e^{\hat{x}} + e^{\hat{x}} \int_0^{|\hat{x}|} e^y [W'_0(y) - W_0(y)] dy, \quad (39)$$

where $W_0(\hat{x} \geq 0) = W(x, 0)$. Then, the solution to equation (37) reads

$$W(\hat{x}, \hat{t}) = \int_{\mathbb{R}} dy W_0(y) \times \frac{1}{\sqrt{4\pi\hat{t}}} \exp\left\{-\frac{(\hat{x}-y)^2}{4\hat{t}}\right\}; \quad (40)$$

this expression is used for $\hat{x} > 0$. Once we have computed W , we obtain the ionic density through

$$\hat{n}_{PNP}(\hat{x}, \hat{t}) = \partial_{\hat{x}}^2 [-\ln W(\hat{x}, \hat{t})], \quad (41)$$

which follows from the Cole–Hopf transformation and Poisson’s equation. The asymptotic behavior as $\hat{t} \rightarrow \infty$ of the PNP density profile is given by the PB solution: $\hat{n}_{PNP}(\hat{x}, \hat{t} \rightarrow \infty) = \hat{n}_{PB}(\hat{x})$.

We now focus on an initially localized density profile $\hat{n}_{PNP}(\hat{x}, 0) = \delta(\hat{x})$, which leads to the following W function:

$$W(\hat{x}, \hat{t}) = \text{erf}\left(\frac{\hat{x}}{2\sqrt{\hat{t}}}\right) - e^{\hat{t}+\hat{x}} \text{erf}\left(\frac{2\hat{t}+\hat{x}}{2\sqrt{\hat{t}}}\right) + e^{\hat{t}+\hat{x}}. \quad (42)$$

The previous expression has to be handled with caution since in general spatial and time limits cannot be exchanged, see equation (36). We can then analyze the asymptotic time behavior of equation (42) by computing the large time expansion:

$$W(\hat{x}, \hat{t}) \underset{\hat{t} \rightarrow \infty}{\sim} \frac{1+\hat{x}}{\sqrt{\pi\hat{t}}} + \mathcal{O}(\hat{t}^{-3/2}). \quad (43)$$

The mean-field density profile follows, as

$$\hat{n}_{PNP}(\hat{x}, \hat{t}) = \frac{e^{-\hat{x}^2/4\hat{t}}}{\sqrt{\pi\hat{t}} \left[\text{erf}\left(\frac{\hat{x}}{2\sqrt{\hat{t}}}\right) + e^{\hat{t}+\hat{x}} \text{erfc}\left(\frac{2\hat{t}+\hat{x}}{2\sqrt{\hat{t}}}\right) \right]} - \frac{e^{\hat{t}+\hat{x}} \text{erf}\left(\frac{\hat{x}}{2\sqrt{\hat{t}}}\right) \text{erfc}\left(\frac{2\hat{t}+\hat{x}}{2\sqrt{\hat{t}}}\right)}{\left[\text{erf}\left(\frac{\hat{x}}{2\sqrt{\hat{t}}}\right) + e^{\hat{t}+\hat{x}} \text{erfc}\left(\frac{2\hat{t}+\hat{x}}{2\sqrt{\hat{t}}}\right) \right]^2}, \quad (44)$$

which admits the following expansion at large times

$$\hat{n}_{PNP} \underset{\hat{t} \rightarrow \infty}{\sim} \frac{1}{(1+\hat{x})^2} \left[1 + \frac{\hat{x}^3 + 3\hat{x}^2 + 3\hat{x} + 3}{6(\hat{x}+1)\hat{t}} + \mathcal{O}\left(\frac{1}{\hat{t}^{3/2}}\right) \right], \quad (45)$$

where the equilibrium distribution $\hat{n}_{PB}(\hat{x})$ is ultimately reached, as anticipated. The next leading order decays as inverse time, and reveals that the corrections to PB are of order $\sim \hat{x}^2/\hat{t}$ at large distances; this indicates that the tails take longer to converge toward equilibrium. Furthermore, it implies that it takes a time $\hat{t} \sim \hat{x}^2$ for the distribution to reach equilibrium at distance \hat{x} from the colloid. Figure 17 shows how the

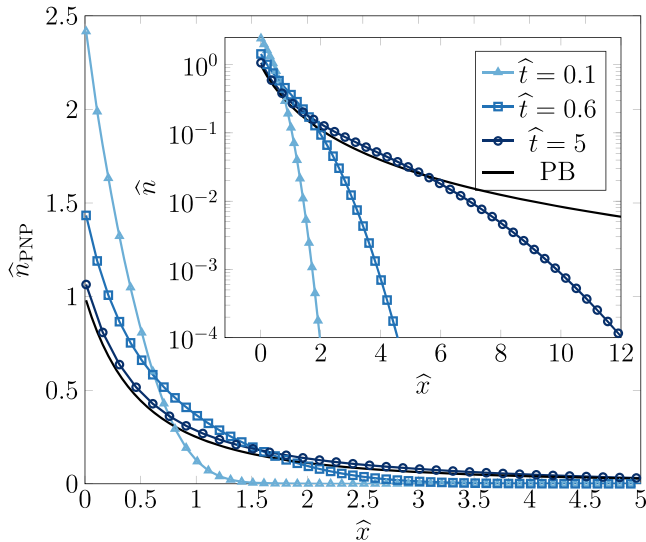


Figure 17. Ionic density at times $\hat{t} = 0.1, 0.6, 5$ for the PNP mean-field dynamics (markers) and the equilibrium PB solution (solid). The IC is $\hat{n}_{\text{PNP}}(\hat{x}, 0) = \delta(\hat{x})$. For $\hat{t} = 5$, the dynamical PNP solution is close to its equilibrium counterpart. The inset shows the same plot in linear–log scale to emphasize the tails of the distributions, where lies the largest difference between PB and PNP at large times.

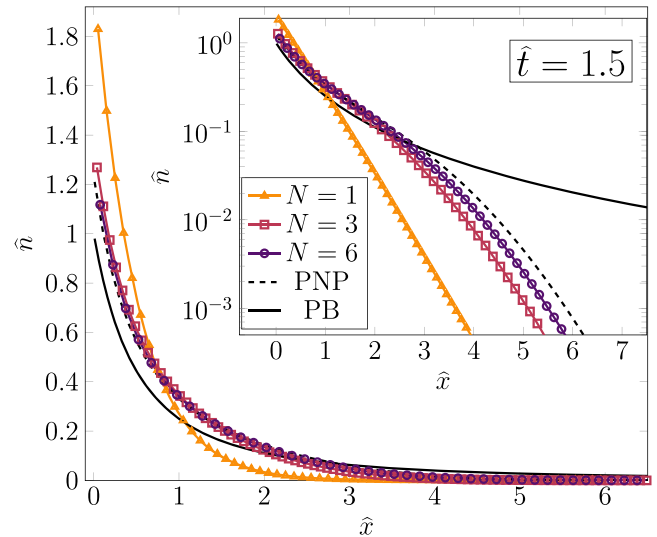


Figure 18. Ionic density at time $\hat{t} = 1.5$, for the PNP mean-field dynamics (dashed) and the discrete N counterion simulation with $N = 1, 3, 6$ (markers). The IC for the different cases consists of all the particles localized at $\hat{x} = 0$. The equilibrium PB mean-field solution \hat{n}_{PB} (solid) is given for reference. The insets show the ionic density in logarithmic scale to magnify the behavior on the tails, where the discrete case departs from the PNP solution.

PNP solution approaches the equilibrium distribution: starting by the region close to the colloid and then spreading outwards. Equation (44) also admits an expansion when $\hat{x} \rightarrow \infty$:

$$\hat{n}_{\text{PNP}} \underset{\hat{x} \rightarrow \infty}{\sim} \frac{e^{-\hat{x}^2/4\hat{t}}}{\sqrt{\pi\hat{t}}} \left[1 - \frac{2\hat{t}}{\hat{x}} + \mathcal{O}\left(\frac{1}{\hat{x}^2}\right) \right], \quad (46)$$

which shows that for a finite time, the distribution has Gaussian tails. Then, the algebraic decay is featured exclusively at equilibrium.

We move on to compare the dynamics of the discrete counterion model and the PNP solution. In figures 18 and 19, the exact discrete results are plotted at different times. For as few as $N = 3$ counterions, the mean-field theory becomes operational, if we exclude the tail. Besides, the larger N , the closer to mean-field the tail behaves.

Finally, we discuss the characteristic relaxation time. The absence of an exponential decay means, that the PNP dynamics is ruled by an infinite characteristic time. To see how this matches with the finite N exact results, we examine how the characteristic time $\hat{\tau}$ behaves when N increases while keeping the colloid charge Ne ($2Q = N$ in the discrete case) fixed. For $L = 0$, we have found $\hat{\tau} \sim 4$, for even and odd values of N . This means that $\hat{\tau} \sim N^2$. Therefore, in the mean-field limit $N \rightarrow \infty$ and $e \rightarrow 0$ with fixed Ne , the characteristic time diverges, to yield the PNP result of a diverging scale. Figure 20 illustrates how an observable, the KLD, approaches the mean-field as N increases while keeping Ne fixed.

5. Misfit counterion transport time

We have seen that the relaxation dynamics depends on whether the number of ions is even or odd, with the slowest relaxation

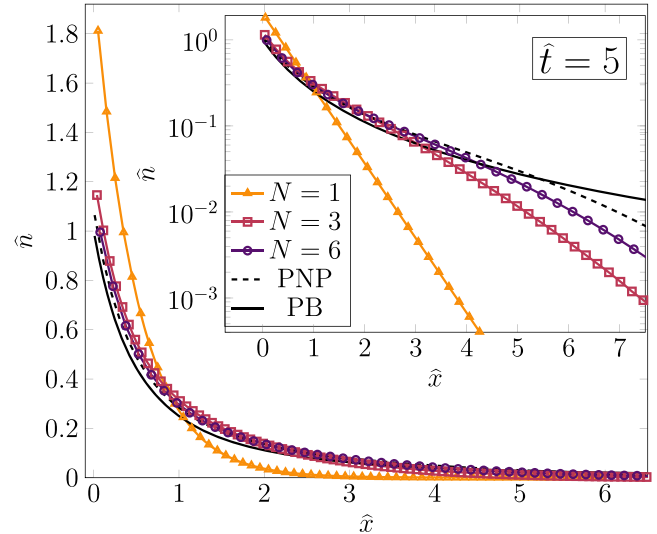


Figure 19. Same as figure 18 with $\hat{t} = 5$.

occurring in the odd case. In order to investigate this further, let us revisit the case where we have an odd number of counterions $N = 2M - 1$ with $M > 1$, and focus on the misfit ion. This misfit ion already plays an important role in the thermal equilibrium properties in 3D systems [58], therefore it is interesting to understand also its role in the dynamical properties. If we label the ions from 1 to N according to their increasing position, the misfit ion is the middle one or M th ion. Due to the nature of 1D Coulomb interactions and the charge neutrality of the system, there is no net drift force acting on the M th ion whenever it lies between the two colloids. As a result, it undergoes free Brownian motion until it collides with either of its neighbors.

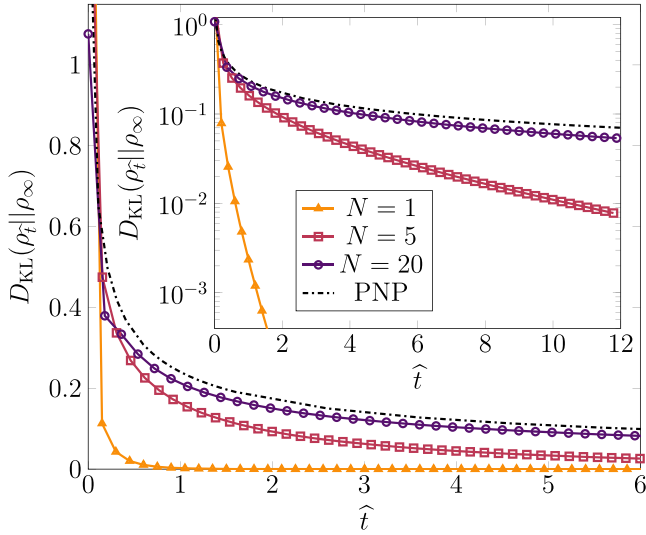


Figure 20. KLD for $N = 1, 5, 20$ (marks) and for the PNP mean-field dynamical solution (dashdotted). The KLD is taken between the dynamical distribution and its corresponding equilibrium state. Note how this observable converges to the PNP curve as the number of counterions increases.

5.1. Transport time distribution

We consider the time and distance between collisions of the M th ion with its neighbors as follows. Suppose that the system is in equilibrium and that the misfit ion collides with, say, the $(M - 1)$ th ion (its left neighbor). We record the time and position of this collision and let the system evolve until the M th ion collides with its right neighbor (the $(M + 1)$ th ion). We then calculate the time interval and distance between collisions. Finally, we record the position and time of this new collision and repeat the process for the next collision with the $(M - 1)$ th ion. In this manner, we record 10^6 samples of times and distances, obtaining the corresponding sample averages and standard deviations. Note that we do not record data from successive collisions with the same neighbor. For example, after recording a collision with the left neighbor, we do not record any new collisions with the left neighbor until a collision with the right neighbor has occurred. In doing so, we define the transport time distribution between double-layers.

With $N = 25$, the time between collisions is distributed as shown in figure 21. We observe that for $\tilde{L} = 3$ the collision times take mostly small values, while for $\tilde{L} \geq 7$ the distributions show noticeably longer tails, indicating that the M th ion requires a much longer time to go from one of its neighbors to the other. Besides, it is seen in figure 21 that the short-time collision probability diminishes as \tilde{L} increases. This is due to the minimum distance the counterion needs to find another particle: at large \tilde{L} , all ions except the misfit are located in the vicinity of the colloids. The misfit thus needs to travel a distance of order \tilde{L} to collide with a new partner (see more details below). We then calculate the average transport time; the results, shown in figure 22(a) do exhibit the expected diffusive \tilde{L}^2 scaling for large \tilde{L} .

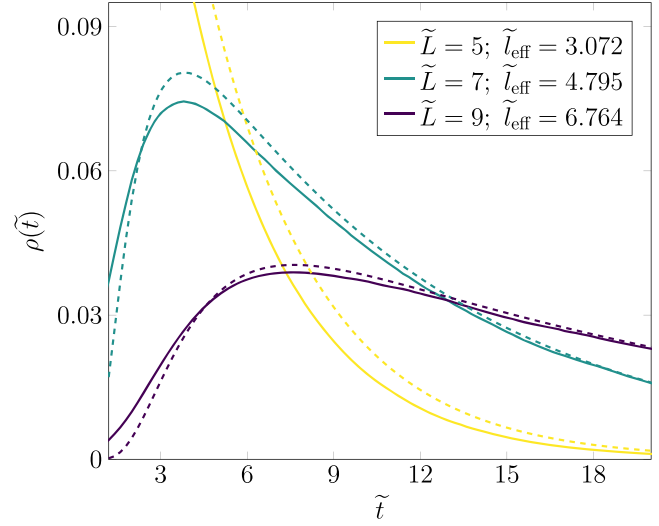


Figure 21. Transport time distribution for the misfit ion (solid lines) and fitted fixed wall model time distribution $q_{\tilde{L}_{\text{eff}}}(\tilde{t})$ (dashed lines), for $N = 25$.

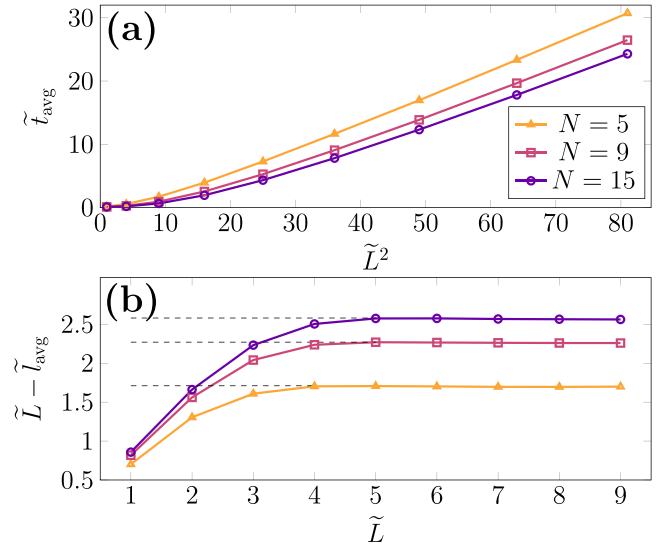


Figure 22. (a) Average transport time as a function of \tilde{L}^2 . The lines are guides to the eye. (b) Difference $\tilde{L} - \tilde{t}_{\text{avg}}$ for $N = 5, 9$ and 15 . The lines are guides to the eye and the horizontal dashed lines show the asymptotic value as $\tilde{L} \rightarrow \infty$. The equivalent plot for $\tilde{L} - \tilde{t}_{\text{eff}}$ (not shown) yields a similar behavior: a bounded monotonic increase to a slightly different terminal value, yet reaching it nearly for the same \tilde{L} .

5.2. Effective model for the misfit's free space

We are interested in estimating the length of the available free space for the misfit. This is expected to be given by \tilde{L} minus two double-layer sizes (one on the right, another on the left-hand side). While we do not have the explicit form of the collision time distribution as a function of \tilde{L} , we can resort to the boxed particle model introduced in section 2.4. We then estimate the transport time as a function of the distance between walls \tilde{l} , namely $\tau_{\tilde{l}}$, as given in (24). We present a derivation of its distribution in appendix D. Using this object, we can investigate the effective size of the system between the ion clouds

using the M th ion as a probe. We perform a parameter fit to find the value of l for which $q_{\tilde{l}}(\tilde{t})$, which is the transport distribution (equation (25)) for a Brownian particle in a 1D box of length \tilde{l} , reproduces the collision time distributions most closely, and we denote it by \tilde{l}_{eff} . The result of the parameter fit is shown in figure 21; as expected, the fixed wall model time distribution seems to reproduce the transport time distribution more closely as \tilde{L} grows.

The first observation to be made about $q_{\tilde{l}}(\tilde{t})$ as expressed in equation (25) is that it obeys the scaling relation

$$q_{\tilde{l}}(\tilde{t}) = \tilde{l}^{-2} \mathcal{Q}\left(\frac{\tilde{t}}{\tilde{l}^2}\right), \quad (47)$$

where $\mathcal{Q}(t)$ is a scaling function. This means time scales like \tilde{l}^2 . Indeed,

$$\int_0^\infty \tilde{t} q_{\tilde{l}}(\tilde{t}) d\tilde{t} = \frac{\tilde{l}^2}{2}. \quad (48)$$

For large enough \tilde{L} , this quadratic behavior is observed in figure 22(a).

For smaller values of \tilde{L} , the boxed particle model fails to describe the situation. The behavior of $\tilde{L} - \tilde{l}_{\text{eff}}$ as a function of \tilde{L} , resembles the one featured for \tilde{l}_{avg} (figure 22(b)). After calculating the coefficient of determination R^2 of each fit, we find that its value is quite low (less than 0.5 in several cases) for $\tilde{L} < 5$, while it lies consistently between 0.75 and 1 and shows a monotonically increasing behavior when $\tilde{L} \geq 5$, that is, the fits become more reliable as \tilde{L} grows. Moreover, with increasing \tilde{L} , $\tilde{L} - \tilde{l}_{\text{eff}}$ tends to a value that depends only on N , and as N grows this value converges to a limit close to 2; this limit is roughly twice the double-layer size, which in the non-permeable case is exactly 1 [51]. To see this, we examined $\tilde{L} - \tilde{l}_{\text{eff}}$ as a function of N^{-1} . The $\tilde{L} - \tilde{l}_{\text{eff}}$ behaves as a linear function of N^{-1} as $N \rightarrow \infty$, which allows to extrapolate the asymptotic behavior

$$\lim_{N \rightarrow \infty} (\tilde{L} - \tilde{l}_{\text{eff}}) = 2.46 \pm 0.01. \quad (49)$$

Finally, let us analyze directly the distribution of distances traveled by the misfit ion between collisions. In figure 23, we show the results for a system of 25 counterions. When $\tilde{L} = 3$, a large fraction of the collisions occur at very small distances (less than 0.5) which results in a peak at the origin. For $\tilde{L} \geq 7$, the distribution has no such peak. We also observe that as \tilde{L} increases, the distribution shifts to the right without significant changes in the shape. We define \tilde{l}_{avg} as the average of the collision distance data, that is, the mean of the collision distance distributions depicted in figure 23. Performing a similar analysis as for \tilde{l}_{eff} yields similar asymptotic results for growing \tilde{L} , see figure 22(b). By considering the difference $\tilde{L} - \tilde{l}_{\text{avg}}$ for $\tilde{L} = 5$ as a function of $1/N$, we observe that \tilde{l}_{avg} converges to a well-defined value, as N tends to infinity. Similar to the behavior of $\tilde{L} - \tilde{l}_{\text{eff}}$, we see that $\tilde{L} - \tilde{l}_{\text{avg}}$ is a linear function of N^{-1} as $N \rightarrow \infty$. From the fit we obtain

$$\lim_{N \rightarrow \infty} [\tilde{L} - \tilde{l}_{\text{avg}}(N, \tilde{L})] = 3.05 \pm 0.01. \quad (50)$$

As before, we expect this value to only vary slightly and converge as $\tilde{L} \rightarrow \infty$ in the same way as $\tilde{L} - \tilde{l}_{\text{eff}}$.

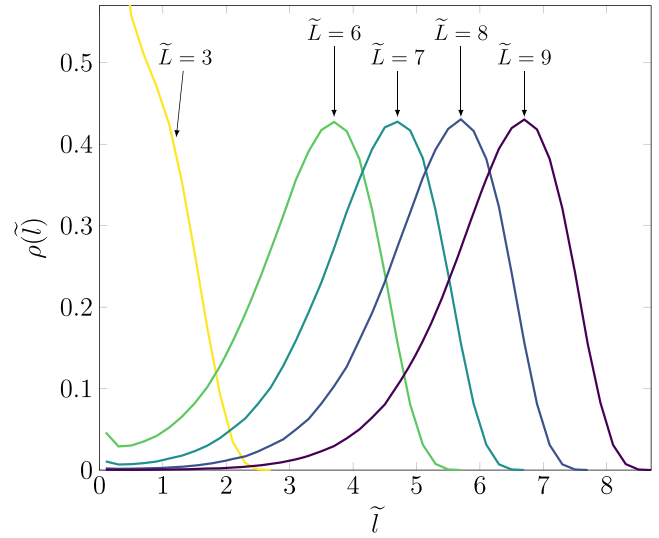


Figure 23. Distribution of distances traveled by the misfit ion between the double-layers, for $N = 25$ and various \tilde{L} .

5.3. Misfit's role in the relaxation time

In view of the analysis in section 2, we expect the characteristic time to be a quadratic function of \tilde{L} when the latter is sufficiently large. In addition, equation (11) indicates that the smallest discrete eigenvalue appears when $\tilde{L} \geq \pi$ for $N = 1$. In the present case, we may expect a similar behavior, whenever the free space available to the M th counterion exceeds π ; this length can be estimated by \tilde{l}_{avg} . As can be seen in figure 24, the behavior of $\tilde{\tau}$ in \tilde{l}_{avg}^2 is well obeyed. More specifically, we get for AICs

$$\tilde{\tau}(N, \tilde{L}) = A + B \tilde{l}_{\text{avg}}(N, \tilde{L})^2, \quad (51)$$

with $A = 1.47 \pm 0.18$, $B = 0.107 \pm 0.005$, and $\tilde{L} \geq 7$. Note that the coefficient B is very close to the value predicted by equation (13), which is $1/\pi^2 \approx 0.101$. The curves in figure 11 plotted as functions of \tilde{l}_{avg} are also shown in figure 24, and we see that the characteristic time follows a single curve that does not depend on the number of counterions, provided it is odd. We observe that with the AICs, for all curves, the characteristic time is close to 4 when $\tilde{l}_{\text{avg}} \leq \pi - 1$, and that $\tilde{\tau}$ follows a quadratic growth when $\tilde{l}_{\text{avg}} \geq \pi + 1$.

We perform the same analysis for the SIC, reaching similar conclusions, see figure 24 [71]. Equation (51) is still obeyed, with $A = 0.89 \pm 0.18$ and $B = 0.0252 \pm 0.0012$. Again, the coefficient B is consistent with the asymptotics given by equation (14), which indicate a value of $1/(4\pi^2) \approx 0.0253$. Assuming in addition that the single counterion situation subsumes the key effects, we expect from equation (12) an increasing behavior when $\tilde{l}_{\text{avg}} \geq 3\pi$; this is confirmed by the figure. Moreover, when $\tilde{l}_{\text{avg}} \leq 3$ the characteristic times seem to be independent of the number of ions, and very close to the completely-continuous spectrum value of 4 found for $N = 1$.

The non-monotonicity of the characteristic time shown in figure 24 for AIC with $2 \leq \tilde{l}_{\text{avg}} \leq 4$, and for SIC with $3 \leq$

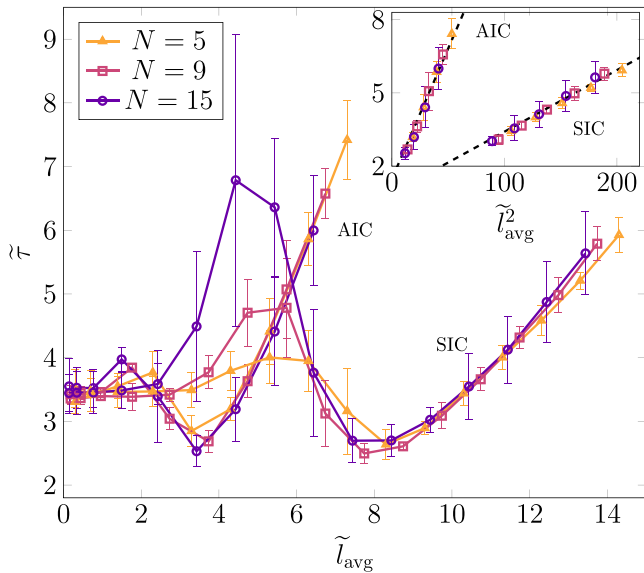


Figure 24. Characteristic time for the AIC and SIC initial conditions as a function of \tilde{l}_{avg} . The straight lines are guides to the eye, and the error bars denote one standard deviation. In the inset, we plot the characteristic time as a function of \tilde{l}_{avg}^2 ; the dashed lines correspond to linear fits.

$\tilde{l}_{\text{avg}} \leq 9$ may be the consequence of the finite number of samples taken during our simulations as well as the finite simulation time. As seen in figure 6, the characteristic time estimated from simulations is quite close to the exact curves when $N = 1$, but it can be observed that $\tilde{\tau}$ is underestimated at small \tilde{L} ; also, estimations made for $N = 1$ in a time interval and a noise level close to those used for $N > 1$ reveal a similarly non-monotonic behavior in the intermediate \tilde{L} region, which we know is nonexistent in the exact $N = 1$ results. We conclude that these non-monotonocities are numerical artifacts, see also the end of appendix C.

6. Conclusion

We have determined the relaxation time τ of an overdamped electroneutral two-colloid system as a function of the colloid separation L and the number of counterion N . The parity of N determines whether τ depends on the distance between colloids. For N odd, we found a behavior that mirrors the single counterion case: $\tau \propto L^2/D$, where D is the diffusion coefficient. From the Stokes–Einstein relation, D grows linearly with temperature (T_{bath}), so that here, τ decreases upon increasing T_{bath} . On the other hand, for N even, $\tau \propto l_B^2/D$ where l_B is the Bjerrum length, which provides a measure of the extension of the equilibrium double-layer in 1D [51]. Since $l_B \propto T_{\text{bath}}$, we conclude that τ increases when increasing T_{bath} : this is due to the enhancement of the double-layer size, under the influence of thermal agitation. The quasi-independence of double-layer size on N —ionic charges being fixed, and therefore at varying colloidal charge—is at the root of the rather striking independence of τ on the number of counterions, when this quantity is an even integer. The irrelevance of N , interestingly, is also observed for N odd, stemming from

a distinct mechanism. There, what matters is the presence of a misfit counterion, that will be, by and large, the dynamical limiting factor. By symmetry, this central ion does not experience any force, while all other ions are subject to a non-vanishing electric field. For large L , this ion diffuses in a domain of size L ; hence the scaling in L^2/D for the characteristic time. Leaving aside the misfit ion, odd- N systems behave much like even ones, and equilibrate over a common time scale l_B^2/D .

We showed that the analytical solution for the mean-field dynamics (namely, the PNP electrokinetic equations) provides a reasonable approximation for a system with as few as $N = 3$ counterions (see figures 18 and 19). We can surmise that the mean-field framework becomes exact in the limit $N \rightarrow \infty$. While the exact equilibrium density profiles at finite- N feature an exponential tail at large distances, their mean-field expressions are longer range, with an algebraic decay. This translates into an infinite characteristic time for equilibration at mean-field level. We have shown that the finite- N finite- τ results did approach this limit as $\tau \propto l_B^2/D \propto e^{-2}$ where e is the charge of the counterions. Since the mean-field limit, for a colloidal object of charge Q , is met for $N \rightarrow \infty$, electroneutrality $Q = 2Ne$ requires that $e \rightarrow 0$. Thus, $\tau \propto e^{-2}$ becomes infinite in the mean-field limit.

Acknowledgments

We would like to thank A Chepelianskii, S Majumdar and L Šamaj for useful discussions. This work was supported by an ECOS-Nord/Minciencias C18P01 action of Colombian and French cooperation. LV and GT acknowledge support from Fondo de Investigaciones, Facultad de Ciencias, Universidad de los Andes, Program INV-2019-84-1825 and Exacore HPC Uniandes for providing high performance computing time. LV acknowledges support from Action Doctorale Internationale (ADI 2018) de l’IDEX Université Paris-Saclay. SA is supported by the JSPS Kakenhi Grant No. JP19K14617.

Data availability statement

All data that support the findings of this study are included within the article (and any supplementary files).

Appendix A. Dry friction in a wedge potential

This section deals with the limit $L \rightarrow 0$, where the system is described by the same equation as that ruling the velocity distribution of Brownian motion with dry friction [60, 61]. The latter describes a particle under the influence of a Langevin force $\xi(t)$ with Gaussian distribution characterized by $\langle \xi(t) \rangle = 0$ and $\langle \xi(t)\xi(0) \rangle = m^2\Gamma\delta(t)$. There is also a dry friction force term of magnitude Δ_F . For our purpose, we only mention the results obtained in the ‘partly stuck’ regime, in which the friction coefficient is small enough to avoid getting stuck but large enough to differ from free Brownian motion. The equation of

motion in that case is given by:

$$m\dot{v} + m\gamma v = -\Delta_F \text{sgn}(v) + \xi(t). \quad (\text{A1})$$

If the viscous damping is neglected ($\gamma \rightarrow 0$), this equation becomes:

$$\dot{v} = -\Delta \text{sgn}(v) + \frac{1}{m}\xi(t), \quad (\text{A2})$$

where $\Delta = \Delta_F/m$ and $\text{sgn}(x)$ is the sign function. The previous equation has an associated Fokker–Planck formulation, which we write in terms of the dimensionless variables $\tilde{x} = 2\Delta v/\Gamma$ and $\tilde{t} = 2\Delta^2 t/\Gamma$:

$$\frac{\partial p(\tilde{x}, \tilde{t}|\tilde{x}_0, 0)}{\partial \tilde{t}} = \frac{\partial}{\partial \tilde{x}} \left(p(\tilde{x}, \tilde{t}|\tilde{x}_0, 0) \text{sgn}(\tilde{x}) \right) + \frac{\partial^2 p(\tilde{x}, \tilde{t}|\tilde{x}_0, 0)}{\partial \tilde{x}^2}, \quad (\text{A3})$$

where $p(\tilde{x}, \tilde{t}|\tilde{x}_0, 0)$ is the propagator for the velocity distribution with initial dimensionless velocity \tilde{x}_0 at a time $\tilde{t}_0 = 0$. Note that the analogy with equation (3) for $\tilde{L} = 0$. This Fokker–Planck equation has been solved using an eigenfunction expansion in [61], which is the same treatment we used for an arbitrary \tilde{L} . Simplifications ensue for $\tilde{L} = 0$ and a closed form expression is available:

$$p(\tilde{x}, \tilde{t}|\tilde{x}_0, 0) = \frac{1}{2\sqrt{\pi\tilde{t}}} e^{-\tilde{t}/4} e^{-(|\tilde{x}|-|\tilde{x}_0|)/2} e^{-(\tilde{x}-\tilde{x}_0)^2/4\tilde{t}} + \frac{e^{-|\tilde{x}|}}{4} \left[1 + \text{erf} \left(\frac{\tilde{t} - |\tilde{x}| - |\tilde{x}_0|}{2\tilde{t}^{1/2}} \right) \right], \quad (\text{A4})$$

where $\text{erf}(x)$ is the error function. This density distribution explicitly shows the time scale $\tau = 2m^2\Gamma/\Delta_F^2$ (or $\tilde{\tau} = 4$ in dimensionless units).

The constant drift diffusion described in previous sections is observed directly from the average position:

$$\langle \tilde{x}(\tilde{t}) \rangle = \text{sgn}(\tilde{x}_0) \left[\left(\frac{|\tilde{x}_0| - \tilde{t}}{2} \right) \text{erfc} \left(\frac{\tilde{t} - |\tilde{x}_0|}{2\tilde{t}^{1/2}} \right) + e^{|\tilde{x}_0|} \left(\frac{|\tilde{x}_0| + \tilde{t}}{2} \right) \text{erfc} \left(\frac{\tilde{t} + |\tilde{x}_0|}{2\tilde{t}^{1/2}} \right) \right], \quad (\text{A5})$$

where $\text{erfc}(x)$ is the complementary error function. The previous expression can be shown to follow a ballistic behavior $\langle \tilde{x}(t) \rangle \approx \tilde{x}_0 - \tilde{t} \text{sgn}(\tilde{x}_0)$ during the period $\tilde{t} < \tilde{x}_0$ ($t < v_0/\Delta$). After this, the average velocity decays exponentially to 0.

Appendix B. Fokker–Planck equation for $N = 1$

The eigenfunctions u of the Fokker–Planck operator follow from solving:

$$\frac{d^2 u(\tilde{x}, \lambda)}{d\tilde{x}^2} + \frac{d}{d\tilde{x}} \left(\tilde{\Phi}'(\tilde{x}) u(\tilde{x}, \lambda) \right) + \lambda u(\tilde{x}, \lambda) = 0, \quad (\text{B1})$$

where the eigenvalue λ is real and positive. This result stems from the fact that the 1D Fokker–Planck equation can be transformed to a Schrödinger equation, which involves a Hermitian operator and therefore a real spectrum [62, 63]. Furthermore,

the potential is confining enough to allow for a localized steady state.

The eigenproblem equation (equation (B1)) is piece-wise in three regions: $\tilde{x} < -\tilde{L}/2$, $-\tilde{L}/2 < \tilde{x} < \tilde{L}/2$ and $\tilde{x} > \tilde{L}/2$. For that reason, equation (B1) is solved for each region, with

$$u((\tilde{L}/2)^+, \lambda) = u((\tilde{L}/2)^-, \lambda), \quad (\text{B2})$$

$$u'((\tilde{L}/2)^+, \lambda) + u((\tilde{L}/2)^+, \lambda) = u'((\tilde{L}/2)^-, \lambda), \quad (\text{B3})$$

where these equations express the continuity of the eigenfunction and of the probability current $j(\tilde{x}, \lambda) = \tilde{\Phi}'(\tilde{x})u(\tilde{x}, \lambda) + u'(\tilde{x}, \lambda)$ at $\tilde{x} = \tilde{L}/2$, respectively. The interface conditions at $-\tilde{L}/2$ are analogous. Equations (B2) and (B3) only have non-trivial solutions for a discrete set of eigenvalues $\{\lambda_k\}_k$ in the domain $[0, 1/4)$. This set is \tilde{L} -dependent and non-empty since the equilibrium distribution, given by $\lambda_0 = 0$, is always present. On the other hand, the spectrum is continuous in $[1/4, \infty)$, independent of \tilde{L} . We use the notation $u_{\lambda_k}(\tilde{x})$ and $u(\tilde{x}, \lambda)$ for the eigenfunctions of each case respectively. The eigenfunctions of the adjoint problem $v(\tilde{x}, \lambda)$ follow from $v(\tilde{x}, \lambda) = u(\tilde{x}, \lambda)e^{\tilde{\Phi}(\tilde{x})}$, where the discrete case is obtained by adding the corresponding subscripts. Due to the symmetry of equation (B1), it is convenient to solve it using a linear combination of odd and even functions:

$$u^o(|\tilde{x}| < \tilde{L}/2, \lambda) = A^o \sin(\sqrt{\lambda}\tilde{x}) \quad (\text{B4a})$$

$$u^o(|\tilde{x}| > \tilde{L}/2, \lambda) = e^{-\frac{|\tilde{x}|}{2}} [B_1^o \sin(\tilde{x}\beta_\lambda) + B_2^o \text{sgn}(\tilde{x}) \cos(\tilde{x}\beta_\lambda)] \quad (\text{B4b})$$

$$u^e(|\tilde{x}| < \tilde{L}/2, \lambda) = A^e \cos(\sqrt{\lambda}\tilde{x}) \quad (\text{B4c})$$

$$u^e(|\tilde{x}| > \tilde{L}/2, \lambda) = e^{-\frac{|\tilde{x}|}{2}} [B_1^e \text{sgn}(\tilde{x}) \sin(\tilde{x}\beta_\lambda) + B_2^e \cos(\tilde{x}\beta_\lambda)], \quad (\text{B4d})$$

and for the discrete spectrum:

$$u_k^o(|\tilde{x}| < \tilde{L}/2) = C^o \sin(\tilde{x}\sqrt{\lambda_k^o}) \quad (\text{B5a})$$

$$u_k^o(|\tilde{x}| > \tilde{L}/2) = D^o \text{sgn}(\tilde{x}) e^{-|\tilde{x}|(1+\sqrt{1-4\lambda_k^o})/2} \quad (\text{B5b})$$

$$u_k^e(|\tilde{x}| < \tilde{L}/2) = C^e \cos(\tilde{x}\sqrt{\lambda_k^e}) \quad (\text{B5c})$$

$$u_k^e(|\tilde{x}| > \tilde{L}/2) = D^e e^{-|\tilde{x}|(1+\sqrt{1-4\lambda_k^e})/2}, \quad (\text{B5d})$$

where $\beta_\lambda = \sqrt{\lambda - 1/4}$. The continuous eigenvalues are $\lambda > 1/4$ and the discrete ones are $0 \leq \lambda_k^\alpha < 1/4$. The superscripts ‘o’ and ‘e’ give the parity of the eigenfunctions. The constants are found at the end of this appendix. The eigenvalue λ_k^α belongs either to an odd ($\alpha = o$) or even ($\alpha = e$) eigenfunction, and it is a solution to equation (9) (if odd) or equation (10) (if even) in the domain $[0, 1/4)$. These equations result from imposing a vanishing determinant of the linear system made by equations (B2) and (B3) for the

eigenfunctions (equations (B5a)–(B5d)). This ensures a non-trivial solution for the discrete family of constants (C^e, C^o, D^e and D^o).

The normalization constants $Z^\alpha(\lambda)$ and Z_k^α are defined by the relations:

$$Z^\alpha(\lambda)\delta(\lambda - \lambda')\delta_{\alpha\alpha'} = \int_{\mathbb{R}} d\tilde{x} u^\alpha(\tilde{x}, \lambda)\nu^{\alpha'}(\tilde{x}, \lambda') \quad (\text{B6})$$

$$Z_k^\alpha \delta_{\lambda_k^\alpha \lambda_k^{\alpha'}} = \int_{\mathbb{R}} d\tilde{x} u_k^\alpha(\tilde{x})\nu_k^{\alpha'}(\tilde{x}), \quad (\text{B7})$$

which yield the following expressions:

$$Z^o(\lambda) = 2\pi\beta_\lambda(B_1^{o2} + B_2^{o2}) \quad (\text{B8a})$$

$$Z^e(\lambda) = 2\pi\beta_\lambda(B_1^{e2} + B_2^{e2}) \quad (\text{B8b})$$

$$Z_k^o = C^{o2} \left(\frac{\tilde{L}}{2} - \frac{\sin(\sqrt{\lambda_k^o \tilde{L}})}{2\sqrt{\lambda_k^o}} \right) e^{\frac{\tilde{L}}{2}} + \frac{D^{o2} e^{-i\beta_{\lambda_k^o} \tilde{L}}}{i\beta_{\lambda_k^o}} \quad (\text{B8c})$$

$$Z_k^e = C^{e2} \left(\frac{\tilde{L}}{2} + \frac{\sin(\sqrt{\lambda_k^e \tilde{L}})}{2\sqrt{\lambda_k^e}} \right) e^{\frac{\tilde{L}}{2}} + \frac{D^{e2} e^{-i\beta_{\lambda_k^e} \tilde{L}}}{i\beta_{\lambda_k^e}} \quad (\text{B8d})$$

$$Z_\infty = (\tilde{L} + 2)e^{-\tilde{L}/2}, \quad (\text{B8e})$$

where $i\beta_{\lambda_k} = \sqrt{1/4 - \lambda_k}$, and Z_∞ is the partition function for the equilibrium distribution ($\lambda_0 = 0$), which is given by equation (6).

Finally, the following constants are determined by the vanishing boundary conditions at infinity and equations (B2) and (B3). Additionally, for the discrete case, the determinant for the linear system that rules the family of constants must vanish (equations (9) and (10))

$$\frac{B_1^o}{B_2^o} = \frac{2\beta_\lambda + \tan\left(\frac{\tilde{L}}{2}\beta_\lambda\right) \left[1 - 2\sqrt{\lambda} \cot\left(\frac{\tilde{L}}{2}\sqrt{\lambda}\right)\right]}{2\beta_\lambda \tan\left(\frac{\tilde{L}}{2}\beta_\lambda\right) + 2\sqrt{\lambda} \cot\left(\frac{\tilde{L}}{2}\sqrt{\lambda}\right) - 1} \quad (\text{B9})$$

$$\frac{B_1^e}{B_2^e} = \frac{2\beta_\lambda + \tan\left(\frac{\tilde{L}}{2}\beta_\lambda\right) \left[2\sqrt{\lambda} \tan\left(\frac{\tilde{L}}{2}\sqrt{\lambda}\right) + 1\right]}{2\sqrt{\lambda} \tan\left(\frac{\tilde{L}}{2}\sqrt{\lambda}\right) - 2\beta_\lambda \tan\left(\frac{\tilde{L}}{2}\beta_\lambda\right) + 1} \quad (\text{B10})$$

$$\frac{A^o}{B_2^o} = \frac{2\beta_\lambda e^{-\tilde{L}/4} \csc\left(\frac{\tilde{L}}{2}\sqrt{\lambda}\right) \sec\left(\frac{\tilde{L}}{2}\beta_\lambda\right)}{2\beta_\lambda \tan\left(\frac{\tilde{L}}{2}\beta_\lambda\right) + 2\sqrt{\lambda} \cot\left(\frac{\tilde{L}}{2}\sqrt{\lambda}\right) - 1} \quad (\text{B11})$$

$$\frac{A^e}{B_2^e} = \frac{2\beta_\lambda e^{-\tilde{L}/4} \sec\left(\frac{\tilde{L}}{2}\sqrt{\lambda}\right) \sec\left(\frac{\tilde{L}}{2}\beta_\lambda\right)}{2\sqrt{\lambda} \tan\left(\frac{\tilde{L}}{2}\sqrt{\lambda}\right) + 1 - 2\beta_\lambda \tan\left(\frac{\tilde{L}}{2}\beta_\lambda\right)} \quad (\text{B12})$$

$$\frac{D^o}{C^o} = e^{(2i\beta_{\lambda_k^o} + 1)\tilde{L}/4} \sin\left(\tilde{L}\sqrt{\lambda_k^o}/2\right) \quad (\text{B13})$$

$$\frac{D^e}{C^e} = e^{(2i\beta_{\lambda_k^e} + 1)\tilde{L}/4} \cos\left(\tilde{L}\sqrt{\lambda_k^e}/2\right). \quad (\text{B14})$$

Appendix C. Asymptotic Kullback–Leibler divergence for $N = 1$

This appendix computes the asymptotic behavior of the KLD when $N = 1$ (equation (18)). For this purpose it will be useful to realize that δp is the sum of a term that comes from the continuous spectrum (ε_λ) and another from the discrete one ($\sum_{\alpha,k} \varepsilon_{\lambda_k^\alpha}$):

$$\delta p(\tilde{x}, \tilde{t}, \tilde{x}_0) = \varepsilon_\lambda + \sum_{\alpha,k} \varepsilon_{\lambda_k^\alpha}, \quad (\text{C1})$$

where ε_λ and $\sum_{\alpha,k} \varepsilon_{\lambda_k^\alpha}$ are the terms of the ionic density (equation (5)) associated to the continuous ($\lambda \geq 1/4$) and non-zero discrete ($0 < \lambda_k^\alpha < 1/4$) parts of the spectrum respectively. The contribution of ε_λ is always non-zero, while $\sum_{\alpha,k} \varepsilon_{\lambda_k^\alpha}$ can vanish completely depending on \tilde{L} and \tilde{x}_0 .

We start by analyzing the large time behavior of the KLD when the only contribution is due to the continuous spectrum term ε_λ and therefore we have:

$$D_{\text{KL}}(p||p_\infty) \sim \int_{\mathbb{R}} d\tilde{x} \frac{(\varepsilon_\lambda)^2}{p_\infty} = \frac{Z_\infty e^{\frac{\tilde{L}}{2}}}{2\pi} I(\tilde{x}_0, \tilde{L}, t), \quad (\text{C2})$$

where I is the following integral:

$$I = \int_{\frac{1}{4}}^{\infty} d\lambda \frac{(4\sqrt{\lambda} - 2 \sin(\sqrt{\lambda\tilde{L}}) \cos(2\sqrt{\lambda\tilde{x}_0})) e^{-2\lambda\tilde{t}}}{(4\lambda - 1)^{-\frac{1}{2}} \sqrt{\lambda} (8\lambda + \cos(2\sqrt{\lambda\tilde{L}}) - 1)}. \quad (\text{C3})$$

This term is obtained by exchanging the integration order of λ and \tilde{x} , and then calculating the spatial integral. After some algebra, the remaining expression is I , which unfortunately has no closed form. However, it is possible to find lower and upper bounds. Since I is an integral of a positive function, the integral of a function that bounds the integrand is a bound of I . Following this reasoning we find the following inequality

$$e^{-\frac{\tilde{t}}{2}} \left[\frac{1}{\tilde{t}^{\frac{3}{2}}} + \mathcal{O}\left(\frac{1}{\tilde{t}^{\frac{7}{2}}}\right) \right] \leq \frac{\sqrt{8I}}{3\sqrt{\pi}} \leq e^{-\frac{\tilde{t}}{2}} \left[\frac{1}{\tilde{t}^{\frac{1}{2}}} + \mathcal{O}\left(\frac{1}{\tilde{t}^{\frac{3}{2}}}\right) \right]. \quad (\text{C4})$$

This implies that the KLD is dominantly of the form $\exp(-\tilde{t}/2)$ for asymptotically long times. This behavior is not a surprise, since I has an integrand dominated by $\exp(-2\lambda\tilde{t})$ when $\tilde{t} \rightarrow \infty$, which is maximum when λ takes its minimum value $1/4$. The next order correction is a power function term \tilde{t}^{-s} , where $1/2 \leq s \leq 5/2$. For $\tilde{L} = 0$, the explicit calculation is possible, which yields $s = 3/2$. The subdominant term \tilde{t}^{-s} is relevant in practice, due to the limited time domain accessible in the simulations.

We now focus on the situation where $\sum_{\alpha,k} \varepsilon_{\lambda_k^\alpha}$ is non-zero. Discrete branches, featuring smaller eigenvalues, do dominate at long times over their continuous counterpart. Which eigenvalue it is depends on \tilde{L} (as seen in figure 4) and also on the symmetry of the ICs. We summarize all the possible cases, including the previous continuous result, in the

following relation:

$$D_{\text{KL}}(\rho||p_\infty) \sim \begin{cases} \frac{Z_\infty[\nu_1^o(\tilde{x}_0)]^2}{Z_1^o} e^{-2\lambda_1^o \tilde{t}}, & \tilde{L} > \pi, \tilde{x}_0 \neq 0 \\ \frac{Z_\infty[\nu_1^e(\tilde{x}_0)]^2}{Z_1^e} e^{-2\lambda_1^e \tilde{t}}, & \tilde{L} > 3\pi, \tilde{x}_0 = 0 \\ \frac{3Z_\infty e^{\tilde{L}/2}}{4\sqrt{2\pi}} e^{-\tilde{t}/2\tilde{t}^{-s}}, & \text{elsewhere.} \end{cases} \quad (\text{C5})$$

We conclude this appendix with a note on the behavior of these asymptotic relations when used on time domains which do not take large enough values. In this situation it can happen that some subdominant terms are not negligible, as previously stated for the continuous spectrum term ε_λ . It can also lead to problems in the scheme described in section 2.3.1, for the cross-over regions where the dominant term in δp changes from ε_λ to $\sum_{\alpha,k} \varepsilon_{\lambda_k^\alpha}$.

Appendix D. Derivation of the simplified transport time distribution

The distribution of τ_l as defined in equation (24) can be derived following the ideas in [72, ch XII], and we summarize the method here. The probability density function $p_l(t, x)$ for the free Brownian motion we consider, obeys the Fokker–Planck equation

$$\frac{\partial}{\partial t} p_l(t, x) = \frac{\partial^2}{\partial x^2} p_l(t, x). \quad (\text{D1})$$

The boundary conditions of the problem are that of a reflecting wall at the origin and an absorbing wall at $x = l$, but because Brownian motion has left–right symmetry, we can replace the reflecting wall by a second absorbing wall at $x = -l$. Then, we have

$$\text{Initial condition: } p_l(0, x) = \delta(x), \quad (\text{D2})$$

$$\text{Boundary condition: } p_l(t, -l) = p_l(t, l) = 0.$$

The total (integrated) probability is not conserved, and the rate at which it decreases due to adsorption gives the transport time distribution,

$$q_l(t) = -\left. \frac{\partial}{\partial x} p_l(t, x) \right|_{x=-l}^{x=l}. \quad (\text{D3})$$

To solve (D1), we introduce the Laplace transforms

$$\begin{aligned} \varphi_l(s, x) &= \int_0^\infty e^{-st} p_l(t, x) dt \\ \phi_l(s) &= \int_0^\infty e^{-st} q_l(t) dt, \end{aligned} \quad (\text{D4})$$

with $\text{Re}(s) > 0$. Then, the transform of (D3) reads

$$\phi_l(s) = -\left. \frac{\partial}{\partial x} \varphi_l(t, x) \right|_{x=-l}^{x=l}. \quad (\text{D5})$$

Now, the transform of (D1) becomes an ordinary differential equation, which is solved using (D2) to obtain

$$\varphi_l(s, x) = \frac{\tanh(\sqrt{s}l) \cosh(\sqrt{s}x) - |\sinh(\sqrt{s}x)|}{2\sqrt{s}}, \quad (\text{D6})$$

and due to (D5) we get

$$\phi_l(s) = 1/\cosh(\sqrt{s}l). \quad (\text{D7})$$

This transform is inverted using the Mittag–Leffler expansion of cosh,

$$\phi_l(s) = \sum_{n=0}^\infty (-1)^n \frac{4\pi(2n+1)}{(2n+1)^2\pi^2 + 4s^2 l^2}, \quad (\text{D8})$$

and (25) follows from tables of Laplace transforms.

ORCID iDs

Lucas Varela  <https://orcid.org/0000-0001-5929-2835>
 Sergio Andraus  <https://orcid.org/0000-0002-7828-1821>
 Emmanuel Trizac  <https://orcid.org/0000-0002-0166-1076>
 Gabriel Téllez  <https://orcid.org/0000-0002-6357-260X>

References

- [1] Hunter R J 2001 *Foundations of Colloid Science* 2nd edn (Oxford: Oxford University Press)
- [2] Levin Y 2002 *Rep. Prog. Phys.* **65** 1577
- [3] Jönsson B and Wennerström H 2001 *Electrostatic Effects in Soft Matter and Biophysics* ed C Holm, P Kékicheff and R Podgornik (Dordrecht: Kluwer) pp 171–204
- [4] Levin Y 2005 *Physica A* **352** 43
- [5] Caffrey M 2001 *Electrostatic Effects in Soft Matter and Biophysics* ed C Holm, P Kékicheff and R Podgornik (Dordrecht: Kluwer)
- [6] Schoch R B, Han J and Renaud P 2008 *Rev. Mod. Phys.* **80** 839
- [7] Jubin L, Poggioli A, Siria A and Bocquet L 2018 *Proc. Natl Acad. Sci. USA* **115** 4063
- [8] Kavokine N, Marbach S, Siria A and Bocquet L 2019 *Nat. Nanotechnol.* **14** 573
- [9] Drummond T G, Hill M G and Barton J K 2003 *Nat. Biotechnol.* **21** 1192
- [10] Burt R, Birkett G and Zhao X S 2014 *Phys. Chem. Chem. Phys.* **16** 6519
- [11] Simon P and Gogotsi Y 2008 *Nat. Mater.* **7** 845
- [12] Sharma P and Bhatti T S 2010 *Energy Convers. Manage.* **51** 2901
- [13] Merlet C, Rotenberg B, Madden P A, Taberna P-L, Simon P, Gogotsi Y and Salanne M 2012 *Nat. Mater.* **11** 306
- [14] Xu K and Fullerton-Shirey S K 2020 *J. Phys. Mater.* **3** 032001
- [15] Anderson M A, Cudero A L and Palma J 2010 *Electrochim. Acta* **55** 3845
- [16] Grahame D C 1947 *Chem. Rev.* **41** 441
- [17] Verwey E J W, Overbeek J T G and van Nes K 1948 *Theory of the Stability of Lyophobic Colloids: The Interaction of Sol Particles Having an Electric Double Layer* (The Netherlands: Elsevier)
- [18] Ohshima H 2006 *Theory of Colloid and Interfacial Electric Phenomena* 1st edn 12 *Interface science and technology* (The Netherlands: Elsevier)
- [19] Helmholtz H 1879 *Ann. Phys. Chem.* **243** 337
- [20] Gouy M 1910 *J. Phys. Theor. Appl.* **9** 457
- [21] Chapman D L 1913 *London, Edinburgh Dublin Phil. Mag. J. Sci.* **25** 475
- [22] Stern O 1924 *Z. Elektrochem. Angew. Phys. Chem.* **30** 508
- [23] Bikerman J J 1942 *London, Edinburgh Dublin Phil. Mag. J. Sci.* **33** 384
- [24] Freise V 1952 *Z. Elektrochem. Ber. Bunsengesellschaft Phys. Chem.* **56** 822
- [25] Kralj-Iglic V and Iglic A 1996 *J. Phys. II France* **6** 477

- [26] Borukhovich I, Andelman D and Orland H 1997 *Phys. Rev. Lett.* **79** 435
- [27] Kornyshev A A 2007 *J. Phys. Chem. B* **111** 5545
- [28] Frydel D and Levin Y 2012 *J. Chem. Phys.* **137** 164703
- [29] Huang Y, Liu X, Li S and Yan T 2016 *Chin. Phys. B* **25** 016801
- [30] Guldbraand L, Jönsson B, Wennerström H and Linse P 1984 *J. Chem. Phys.* **80** 2221
- [31] Allahyarov E, D'Amico I and Löwen H 1999 *Phys. Rev. E* **60** 3199
- [32] Moreira A G and Netz R R 2002 *Eur. Phys. J. E* **8** 33
- [33] Moreira A G and Netz R R 2001 *Electrostatic Effects in Soft Matter and Biophysics* ed C Holm, P Kékicheff and R Podgornik (Dordrecht: Kluwer) pp 367–408
- [34] Boroudjerdi H, Kim Y, Naji A, Netz R, Schlagberger X and Serr A 2005 *Phys. Rep.* **416** 129
- [35] Naji A, Jungblut S, Moreira A G and Netz R R 2005 *Physica A* **352** 131
- [36] Šamaj L and Trizac E 2011 *Phys. Rev. Lett.* **106** 078301
- [37] Šamaj L, Trulsson M and Trizac E 2018 *Soft Matter* **14** 4040
- [38] Golestanian R 2000 *Europhys. Lett.* **52** 47
- [39] Bazant M Z, Thornton K and Ajdari A 2004 *Phys. Rev. E* **70** 021506
- [40] Morrow R, McKenzie D R and Bilek M M M 2006 *J. Phys. D: Appl. Phys.* **39** 937
- [41] Alexe-Ionescu A L, Barbero G, Freire F C M and Scalerandi M 2006 *Liq. Cryst.* **33** 1177
- [42] Lim J, Whitcomb J, Boyd J and Varghese J 2007 *J. Colloid Interface Sci.* **305** 159
- [43] Højgaard Olesen L, Bazant M Z and Bruus H 2010 *Phys. Rev. E* **82** 011501
- [44] Janssen M and Bier M 2018 *Phys. Rev. E* **97** 052616
- [45] Palaia I, Telles I M, dos Santos A P and Trizac E 2020 *Soft Matter* **16** 10688
- [46] Telles I M and dos Santos A P 2021 *Langmuir* **37** 2104
- [47] Bazant M Z, Kilic M S, Storey B D and Ajdari A 2009 *Adv. Colloid Interface Sci.* **152** 48
- [48] Storey B D and Bazant M Z 2012 *Phys. Rev. E* **86** 056303
- [49] Dean D S, Horgan R R and Sentenac D 1998 *J. Stat. Phys.* **90** 899
- [50] Dean D S, Horgan R R, Naji A and Podgornik R 2009 *J. Chem. Phys.* **130** 094504
- [51] Téllez G and Trizac E 2015 *Phys. Rev. E* **92** 042134
- [52] Varela L, Téllez G and Trizac E 2017 *Phys. Rev. E* **95** 022112
- [53] Trizac E and Téllez G 2018 *Eur. J. Phys.* **39** 025102
- [54] Pellenq R J-M and Van Damme H 2004 *MRS Bull.* **29** 319
- [55] Goyal A, Palaia I, Ioannidou K, Ulm F-J, van Damme H, Pellenq R J-M, Trizac E and del Gado E 2021 *Sci. Adv.* **7** eabg5882
- [56] Palaia I 2019 *PhD Thesis* Université Paris-Saclay <http://theses.fr/2019SACLS398>
- [57] Netz R R 2001 *Eur. Phys. J. E* **5** 557
- [58] Šamaj L, dos Santos A P, Levin Y and Trizac E 2016 *Soft Matter* **12** 8768
- [59] The 1D Coulomb potential $\phi = v_{1D}/(q'q)$ follows from solving Poisson's equation in 1D: $\phi'' = -2\delta(x)/\epsilon$.
- [60] de Gennes P-G 2005 *J. Stat. Phys.* **119** 953
- [61] Touchette H, Van der Straeten E and Just W 2010 *J. Phys. A: Math. Theor.* **43** 445002
- [62] Risken H 1984 *The Fokker–Planck Equation* (Berlin: Springer)
- [63] More precisely, the Fokker–Planck equation is formally equivalent to the time-independent Schrödinger equation with a square well potential of depth $1/4$ with attractive deltas at the colloid positions, for an imaginary time $t_S = -i\hbar t$ and mass $m_S = \hbar^2/2D$ [62]
- [64] Kullback S and Leibler R A 1951 *Ann. Math. Stat.* **22** 79
- [65] Maruyama G 1955 *Rend. Circ. Mat. Palermo* **4** 48
- [66] Milshtein G N 1978 *Theory Probab. Appl.* **23** 396
- [67] For every polynomial function g of the final counterion positions, and every small time step Δt , there exists a positive constant C such that $|\langle g \rangle_{\text{exact}} - \langle g \rangle_{\text{num}}| \leq C\Delta t^{1.0}$
- [68] Kloeden P E and Platen E 1992 *Numerical Solution of Stochastic Differential Equations* (Berlin: Springer)
- [69] Pal S and Pitman J 2008 *Ann. Appl. Probab.* **18** 2179
- [70] Andelman D 2006 *Introduction to Electrostatics in Soft and Biological Matter* (London: Taylor and Francis) pp 97–122
- [71] Since figure 22 shows that $\tilde{L} - \tilde{l}_{\text{avg}}(N, \tilde{L})$ is close to the limiting value at $\tilde{L} = 9$, we use $\tilde{L}_{\text{avg}}(N, \tilde{L}) \approx \tilde{l}_{\text{avg}}(N, 9) + \tilde{L} - 9$ for $\tilde{L} > 9$
- [72] Van Kampen N G 2007 *Stochastic Processes in Physics and Chemistry* 3rd edn (Amsterdam: Elsevier)